85

Preferential concentration driven instability of sheared gas-solid suspensions

M. Houssem Kasbaoui^{1,†}, Donald L. Koch², Ganesh Subramanian³ and Olivier Desjardins¹

¹Sibley School of Mechanical and Aerospace Engineering, Cornell University, Ithaca, NY 14853, USA
²School of Chemical and Biomolecular Engineering, Cornell University, Ithaca, NY 14853, USA
³Engineering Mechanics, JNCASR, Bangalore 560064, India

(Received 30 June 2014; revised 26 January 2015; accepted 28 February 2015; first published online 30 March 2015)

We examine the linear stability of a homogeneous gas-solid suspension of small Stokes number particles, with a moderate mass loading, subject to a simple shear flow. The modulation of the gravitational force exerted on the suspension, due to preferential concentration of particles in regions of low vorticity, in response to an imposed velocity perturbation, can lead to an algebraic instability. Since the fastest growing modes have wavelengths small compared with the characteristic length scale (U_g/Γ) and oscillate with frequencies large compared with Γ , U_g being the settling velocity and Γ the shear rate, we apply the WKB method, a multiple scale technique. This analysis reveals the existence of a number density mode which travels due to the settling of the particles and a momentum mode which travels due to the cross-streamline momentum transport caused by settling. These modes are coupled at a turning point which occurs when the wavevector is nearly horizontal and the most amplified perturbations are those in which a momentum wave upstream of the turning point creates a downstream number density wave. The particle number density perturbations reach a finite, but large amplitude that persists after the wave becomes aligned with the velocity gradient. The growth of the amplitude of particle concentration and fluid velocity disturbances is characterised as a function of the wavenumber and Reynolds number $(Re = U_o^2/\Gamma \nu)$ using both asymptotic theory and a numerical solution of the linearised equations.

Key words: instability, multiphase and particle-laden flows, particle/fluid flow

1. Introduction

A striking feature of the dynamics of inertial particles in gas flows is the tendency of centripetal accelerations to expel the particles from vortical regions so that they preferentially concentrate in straining-dominated regions of the flow (Squires & Eaton 1991). It is natural to expect that the resulting fluctuations in the particle concentration and the forces the particles exert on the fluid will enhance the fluid velocity fluctuations. In this study, we investigate a mechanism by which preferential

concentration of particles and the associated variations in the gravitational forces can lead to enhanced fluid velocity fluctuations in a unidirectional laminar flow. In particular, we consider the linear stability of an unbounded simple shear flow of a homogeneous dilute suspension of inertial particles in a gas, a scenario that allows for a rigorous analysis, but nevertheless extracts mechanisms of growth of concentration fluctuations that are generic and should apply to small-wavelength perturbations in more complicated flow scenarios such as laminar shear mixing layers or turbulent flows. We show that preferential concentration and gravitational forces can lead to a large enhancement in the magnitude of particle concentration and fluid velocity waves as they rotate in the shear flow. The long-term growth of the fluctuations can then arise from the coupled effects of the new preferential concentration instability and the Rayleigh–Taylor instability of stratified particulate flows (Batchelor & Nitsche 1991).

The qualitative physical understanding of the complex dynamics of single-phase fluids is greatly enhanced by the study of a set of classical hydrodynamic instabilities. Our poorer understanding of dispersed multiphase and particulate flows may result then not only from their greater complexity but also from the limited supply of readily understandable instability mechanisms. Many of the classical instabilities of particulate flows, such as the instability of fluidised beds to void fraction waves (Batchelor 1988; Anderson, Sundaresan & Jackson 1995) and the clustering of particles in rapid granular flow (Wang, Jackson & Sundaresan 1996) involve dense flows with particle volume fraction ϕ of order one where the hydrodynamic and collisional interactions among the particles dominate the flow. At the other extreme very dilute flows with small particle mass loading M can be understood with reference to the hydrodynamic instabilities of the carrier fluid. Here, the mass loading is the ratio of the mass supplied by the particles to that supplied by the fluid, i.e. $M = nm/\rho_f$, where n is the number of particles per unit volume, m is the mass of a particle and ρ_f is the density of the fluid. As an example, the dynamics of settling particles in two coflowing gas streams with different velocities is controlled by the Kelvin-Helmholtz instability of the fluid (Tio, GañánCalvo & Lasheras 1993). In addition, the classic approach of Saffman (1962) to the stability of such suspensions is to consider an effective fluid with a density adjusted to take in account the presence of particles.

The most challenging regime is a semi-dilute regime with small particle volume fractions $\phi \ll 1$ but moderate mass loadings M=O(1). In such a regime, the particulate and gas phases play comparable roles in the suspension dynamics. Examples of these flows include the handling of particles in pneumatic conveying (Nishimura & Hunt 2000), methods of contacting gas and solids such as circulating fluidised beds (Dasgupta, Jackson & Sundaresan 1994), and the suspension of particles in dust storms (Alfaro & Gomes 2001). While these applications are influenced by particle-boundary interactions in addition to bulk gas-solid interactions, one can isolate the bulk gas-solid interactions studied here in more idealised experiments such as particle-seeded grid-generated turbulent flows (Aliseda *et al.* 2002) and studies of self-induced turbulence of sedimenting particles (Parthasarathy & Faeth 1990).

In this paper, we analyse the stability of a homogeneous gas-solid suspension in an unbounded simple shear flow. When analysing the evolution of disturbances to unbounded simple shear flows in the form of Fourier modes, it is necessary to account for the turning of the wavevector of the disturbance mode by the imposed shear flow. Kelvin (1887) first analysed the linearised disturbances with turning wavevector, known as Kelvin modes, to the Navier–Stokes equations for unbounded simple shear flow. Interestingly, it has been noted by Craik & Criminale (1986) that each of

these modes, due to its transverse nature, is also a solution to the full Navier–Stokes equations, although a collection of Kelvin modes is not. Lord Kelvin demonstrated that the momentum perturbations eventually decay at long times algebraically in the inviscid case and super-exponentially (exponential of a third-order polynomial) for finite Reynolds numbers. Nevertheless, the modes experience a transient period of algebraic growth which has led to the postulate of the so-called bypass transition to turbulence for shearing flows by a mechanism that couples nonlinear effects with the initial linear transient growth, referred to as 'bootstrapping' (Trefethen *et al.* 1993).

To analyse the stability of unbounded simple shear flow in the presence of a particulate phase, it is necessary to solve equations describing the state of the particulate phase along with mass, momentum and energy conservation equations. Such an analysis has been performed for rapidly sheared granular materials by Schmid & Kytomaa (1994) by solving momentum and kinetic energy conservation coupled with the constitutive equations for a granular material (Lun *et al.* 1984). As in the case of the Navier–Stokes problem, it was found that disturbances in granular materials have a transient period of algebraic growth followed by decay of the disturbances at long times. The extent of the transient growth was much larger for granular materials than for Newtonian fluids leading to an increased possibility that nonlinear effects may arise during the transient period and sustain the disturbed state.

In the present study, we will analyse the coupled linearised dynamics associated with momentum conservation and particle number density conservation in a dilute gas—solid suspension. It will be seen that there is a large algebraic growth of disturbances in this system. In contrast to the cases of single-phase Newtonian flow and granular flows, the number density disturbances in the dilute gas—solid system do not decay at long times but reach a steady amplitude, allowing an indefinite time period for the development of secondary instabilities.

The inertia of the particles, measured by the particle Stokes number $St = \Gamma \tau_p$, plays a critical role in the preferential concentration of particles that is crucial to the instability mechanism studied here. However, to facilitate an analytical development we will consider the case of small but non-zero Stokes number for which Ferry & Balachandar (2001, 2002) have developed a partial differential equation for particle concentration. Here Γ is the shear rate of the imposed flow, $\tau_p = m/(6\pi \mu a)$ is the particle response time, μ is the gas viscosity and a is the particle radius. In the dilute, low-Stokes-number regime, one can neglect the direct hydrodynamic and collisional interactions among the particles, although particles experience indirect interactions through the disturbances to the continuum solution for the fluid velocity induced by the forces exerted by other particles.

We will show that inertially induced preferential concentration of particles combined with their gravitational forcing can destabilise a sheared gas-solid suspension. Evidence that gravity and particle inertia are effective in creating hydrodynamic fluctuations can be gleaned from previous direct numerical simulation (DNS) and experimental studies of turbulent flows. For example, Elghobashi & Truesdell (1993) used forcing to produce isotropic turbulence in a DNS and then introduced particles and observed the decaying turbulence. They found that particles that settle with velocities comparable with the root-mean-square fluid velocity enhance both the turbulent energy and turbulent dissipation rate more than particles experiencing no gravitational force. The enhancement was highest at small wavelengths where the larger scales of turbulence could be viewed as producing shearing flows. Some experimental evidence for particle enhanced hydrodynamic fluctuations comes from

the study of particles in grid generated turbulence by Aliseda *et al.* (2002). It is known from DNS (Wang & Maxey 1993) that particles settle faster in turbulence than in quiescent fluid because the particles are expelled from vortical upwelling regions. Aliseda *et al.* (2002) found that the sedimentation velocity increased with increasing mass loading suggesting that the particles increased the fluid velocity fluctuations and thereby enhanced their own sedimentation.

In this paper, we will analyse the linear stability of a uniformly sheared unbounded gas-solid suspension with a uniform number density. To account for particle inertia and particle-gas coupling we consider a small but finite Stokes number and a moderate mass loading. The particular case of horizontal shear will be investigated, since it is most relevant to flows such as wind-driven dust flow and pneumatic conveying. In § 2, we derive the linearised equations for Fourier-mode velocity and concentration disturbances with wavevectors that turn in the imposed shear flow. From numerical integration of these equations, we observe that the solutions exhibit multiple time scales when the wavelength is much smaller than the characteristic distance $L = U_{\nu}/\Gamma$ over which a particle settles during the shearing time $1/\Gamma$, where U_g is the particle settling velocity. In this case the number density and velocity waves undergo many periods of oscillation due to settling of particles and transport of momentum by particle settling in the time it takes the waves to turn in the shear flow. Since these high-wavenumber disturbances have the largest growth, they are analysed in more detail using the WKB method of multiple time scale analysis. The WKB analysis for inviscid and viscous solutions is presented in §§ 3 and 4, respectively. The analysis reveals the existence of two perturbation modes, which we term the momentum and number density modes. These modes evolve independently for most of their existence. However, the coupling of the two modes in the vicinity of a turning point, when the wavevector is nearly vertical, plays a crucial role in determining the amplitude of the final number density disturbance created by an initial fluid velocity disturbance. A concluding perspective on the study is given in § 5.

2. Derivation of the governing equations

2.1. Derivation of the nonlinear equations

We assume that the particles are small enough that they experience a hydrodynamic force that equals the Stokes drag force as well as a gravitational force. For a solid–gas suspension, the Basset history force and the lift force can be neglected due to the large density ratio. The particle equation of motion is then

$$\frac{\mathrm{d}\boldsymbol{v}}{\mathrm{d}t} = \frac{\boldsymbol{u} - \boldsymbol{v}}{\tau_p} + \boldsymbol{g} \tag{2.1}$$

where v is the particle velocity and u is the fluid velocity. Because we consider small volume fractions, particle-particle collisions are also neglected. The particles act on an incompressible Newtonian fluid through a body force term equal to the number of particles per unit volume times the particle-fluid interaction force (Druzhinin 1995; Ferry & Balachandar 2001). The resulting governing equations for the fluid are

$$\frac{\partial \mathbf{u}}{\partial t} + \mathbf{u} \cdot \nabla \mathbf{u} = -\frac{1}{\rho_f} \nabla p + \nu \nabla^2 \mathbf{u} + \frac{mn}{\rho_f} \frac{\mathbf{v} - \mathbf{u}}{\tau_p}$$
(2.2)

$$\nabla \cdot \boldsymbol{u} = 0. \tag{2.3}$$

In the case of an unbounded shear flow, for which we write the velocity gradient tensor as $\nabla u_b = \Gamma e_2 e_1$, the only characteristic length in the problem is $L = U_g/\Gamma$ where $U_g = \tau_p \mathbf{g}$ refers to the settling velocity of the particles. Note that L represents the distance settled by the particles during the characteristic shearing time. An appropriate Reynolds number for the suspension is then $Re = U_g L/\nu = U_o^2/(\Gamma \nu)$.

While a range of methods can be used to model particles and their interaction with the fluid, Eulerian methods have the advantage of considering the net effect of the particles through spatial fields such as the number density field without requiring the tracking of each individual particle. The number density conservation equation is given by

$$\frac{\partial n}{\partial t} + \nabla \cdot (vn) = 0. \tag{2.4}$$

Equation (2.4) does not include particle diffusion. The diameter of particles large enough to have non-zero Stokes numbers precludes the importance of Brownian diffusion. The suspension is sufficiently dilute to neglect particle collisions and near-field hydrodynamic interactions. Furthermore, the equations already capture the net force exerted by the particles on the fluid so that hydrodynamic diffusion due to point particles would be described by (2.2) and (2.4) provided that the number density fluctuations associated with randomly distributed particles were included in the initial conditions for the number density field.

Starting from the Maxey & Riley (1983) equations of motion for a rigid sphere, Ferry & Balachandar (2001) derived an asymptotic expansion for the particles' velocity in the limit of small Stokes number $St = \Gamma \tau_p \ll 1$. We treat the settling velocity as a leading order contribution to this expansion since U_g is the characteristic velocity scale in the problem. Thus, the expansion up to first order in the particle response time is

$$\boldsymbol{v} = \boldsymbol{u} + \boldsymbol{U}_g - \tau_p \left(\frac{\partial \boldsymbol{u}}{\partial t} + (\boldsymbol{u} + \boldsymbol{U}_g) \cdot \nabla \boldsymbol{u} \right) + O(\tau_p^2). \tag{2.5}$$

The expansion (2.5) is given in dimensional form. When non-dimensionalised by the settling velocity magnitude U_g , the characteristic distance L and the shearing time $1/\Gamma$, it becomes

$$\boldsymbol{v} = \boldsymbol{u} + \boldsymbol{1}_{g} - St \left(\frac{\partial \boldsymbol{u}}{\partial t} + (\boldsymbol{u} + \boldsymbol{1}_{g}) \cdot \nabla \boldsymbol{u} \right) + O(St^{2})$$
 (2.6)

where $\mathbf{1}_g = U_g/U_g$ is a unit vector parallel to gravity. This low-Stokes-number formulation has the advantage that the particle velocity can be related to the local fluid velocity and its derivatives, whereas the flow history along individual particle trajectories must be accounted for at finite Stokes numbers. Note that when St = 0, the particles move with the fluid velocity, acting as tracers. For small but finite Stokes numbers, the particles deviate from the fluid motion because of the fluid acceleration in a reference frame that translates with the sum of the fluid and settling velocities. It has been shown in Ferry & Balachandar (2002) that the above expression is in excellent agreement with a Lagrangian treatment of particles in a turbulent channel flow. The particle concentration equation coupled with the particles' velocity field (2.5) was solved by Rani & Balachandar (2003) in isotropic, homogeneous turbulence and found to be in good agreement with results from Lagrangian particle tracking.

Using the expression (2.5) in the governing equations, we derive the fluid equations of motion and the number density conservation equation. Non-dimensionalised by the length scale $L = U_g/\Gamma$, velocity scale U_g , base state number density n_0 and shearing time scale $1/\Gamma$, the equations are

$$\nabla \cdot \mathbf{u} = 0 \tag{2.7}$$

$$(1 + Mn) \left(\frac{\partial \mathbf{u}}{\partial t} + \mathbf{u} \cdot \nabla \mathbf{u} \right) = -\nabla p + \frac{1}{Re} \nabla^2 \mathbf{u} + \frac{Mn}{St} \mathbf{1}_g \cdot (\mathbf{I} - St \nabla \mathbf{u})$$
 (2.8)

$$\frac{\partial n}{\partial t} + \left(\boldsymbol{u} + \boldsymbol{1}_g - St \left(\frac{\partial \boldsymbol{u}}{\partial t} + (\boldsymbol{u} + \boldsymbol{1}_g) \cdot \nabla \boldsymbol{u} \right) \right) \cdot \nabla n = Stn \nabla \boldsymbol{u} : \nabla \boldsymbol{u}$$
 (2.9)

where I is the identity tensor. Note that the suspension appears to have an effective density $\rho_f(1+Mn)$ equal to the sum of the mass densities of the gas and particulate phases. Another striking feature of the momentum equation (2.8) is that in addition to the gravitational force, the particles exert a body force proportional to $-\mathbf{1}_g \cdot \nabla u$. This term arises from the convection of momentum across fluid streamlines by the settling of the particles.

The number density field in (2.9) is convected by the approximate particle velocity field and can change along particle paths as a result of the compressibility of the particle velocity field. The divergence of the particle velocity is $-St\nabla u: \nabla u = -St(S^2 - \Omega^2)$ with $S^2 = \mathbf{S}: \mathbf{S}$ and $\Omega^2 = \mathbf{R}: \mathbf{R}$ being the second invariants of the fluid strain $\mathbf{S} = (\nabla u + \nabla u^T)/2$ and rotation tensors $\mathbf{R} = (\nabla u - \nabla u^T)/2$. A homogeneous shear flow base state does not contribute to the particle density modulation since $\nabla u_b: \nabla u_b = 0$. This is because a simple shear flow has equal portions of straining and rotational motion. It is through a perturbation to the simple shear and the resulting local imbalance between vorticity and extension that one will obtain a non-zero term in the right-hand side of (2.9). In particular, regions of higher vorticity $(\nabla u: \nabla u = S^2 - \Omega^2 < 0)$ will lead to a depletion of particles, while particles aggregate in regions of higher strain $(\nabla u: \nabla u = S^2 - \Omega^2 > 0)$. This process is known as preferential concentration.

The preferential concentration term is order O(St) in (2.9), because to leading order the particle velocity is equal to the sum of the fluid velocity and settling velocity both of which are divergence free. It follows that a uniform number density is unaltered by the O(1) particle velocity field and number density fluctuations arise only at O(St). Thus, we can write n = 1 + Stn'. In terms of the scaled number density fluctuations n', the conservation equations (2.8) and (2.9) at O(St) become

$$(1+M)\left(\frac{\partial \mathbf{u}}{\partial t} + \mathbf{u} \cdot \nabla \mathbf{u}\right) = -\nabla p' + \frac{1}{Re} \nabla^2 \mathbf{u} - M \mathbf{1}_g \cdot \nabla \mathbf{u} + M n' \mathbf{1}_g \qquad (2.10)$$
$$\frac{\partial n'}{\partial t} + \left(\mathbf{u} + \mathbf{1}_g\right) \cdot \nabla n' = \nabla \mathbf{u} : \nabla \mathbf{u} \qquad (2.11)$$

where $p' = p - (M/St)\mathbf{1}_g \cdot \mathbf{r}$ is a reduced pressure adjusted to remove the gravitational forcing of a uniform particle suspension.

2.2. Linear stability analysis

Next, we assume that the fluid velocity includes a small perturbation to the base simple shear flow such that $u = r \cdot \nabla u_b + u'$, with the base velocity gradient tensor

constant and proportional to the shear rate as defined above. Hence, the momentum perturbation satisfies

$$\frac{\partial \mathbf{u}'}{\partial t} + \mathbf{r} \cdot \nabla \mathbf{u}_b \cdot \nabla \mathbf{u}' + \mathbf{u}' \cdot \nabla \mathbf{u}_b + \frac{M}{1+M} \mathbf{1}_g \cdot \nabla \mathbf{u}'$$

$$= -\frac{1}{1+M} \nabla p' + \frac{1}{1+M} \frac{1}{Re} \nabla^2 \mathbf{u}' + \frac{M}{1+M} \mathbf{1}_g n'$$
(2.12)

$$\nabla \cdot \boldsymbol{u}' = 0 \tag{2.13}$$

and the number density equation becomes

$$\frac{\partial n'}{\partial t} + \mathbf{r} \cdot \nabla \mathbf{u}_b \cdot \nabla n' + \mathbf{1}_g \nabla n' = 2 \nabla \mathbf{u}_b : \nabla u'. \tag{2.14}$$

An arbitrary small perturbation of the number density and fluid velocity fields can be decomposed into spatial Fourier modes and so we define the Fourier transform as

$$\hat{n}(t, \mathbf{k}) = \frac{1}{(2\pi)^{3/2}} \int_{\mathbf{r} \in \mathbb{R}^3} n'(t, \mathbf{r}) \exp(-i\mathbf{k} \cdot \mathbf{r}) d\mathbf{r}$$
(2.15)

and the inverse transforms as

$$n'(t, \mathbf{r}) = \frac{1}{(2\pi)^{3/2}} \int_{\mathbf{k} \in \mathbb{R}^3} \hat{n}(t, \mathbf{k}) \exp(i\mathbf{k} \cdot \mathbf{r}) d\mathbf{k}.$$
 (2.16)

The disturbance equations (2.12) and (2.14) become in Fourier space

$$\frac{\partial \hat{n}}{\partial t} - \mathbf{k} \cdot \nabla \mathbf{u}_{b}^{\mathrm{T}} \cdot \nabla_{k} \hat{n} + \mathrm{i} \mathbf{1}_{g} \cdot \mathbf{k} \hat{n} = \mathrm{i} 2 \nabla \mathbf{u}_{b} : \mathbf{k} \hat{\mathbf{u}}
\frac{\partial \hat{\mathbf{u}}}{\partial t} - \mathbf{k} \cdot \nabla \mathbf{u}_{b}^{\mathrm{T}} \cdot \nabla_{k} \hat{\mathbf{u}} + \hat{\mathbf{u}} \cdot \nabla \mathbf{u}_{b} + \mathrm{i} \frac{M}{1 + M} \mathbf{1}_{g} \cdot \mathbf{k} \hat{\mathbf{u}}
= -\mathrm{i} \frac{1}{1 + M} \mathbf{k} \hat{p} - \frac{1}{1 + M} \frac{k^{2}}{R_{g}} \hat{\mathbf{u}} + \frac{M}{1 + M} \mathbf{1}_{g} \hat{n}.$$
(2.17)

For an incompressible fluid, pressure balances the component of the force field along the k direction. The residual force field drives the flow. The operation l - kk projects (2.18) along the direction parallel to the wavefront. The resulting momentum balance in the transverse direction is

$$\frac{\partial \hat{\boldsymbol{u}}}{\partial t} - \boldsymbol{k} \cdot \nabla \boldsymbol{u}_{b}^{\mathrm{T}} \cdot \nabla_{k} \hat{\boldsymbol{u}} = -\left(\boldsymbol{I} - 2\frac{\boldsymbol{k}\boldsymbol{k}}{k^{2}}\right) \nabla \boldsymbol{u}_{b}^{\mathrm{T}} \cdot \hat{\boldsymbol{u}} - \mathrm{i}\frac{\boldsymbol{M}}{1 + \boldsymbol{M}} \mathbf{1}_{g} \cdot \boldsymbol{k} \hat{\boldsymbol{u}}
- \frac{1}{1 + \boldsymbol{M}} \frac{k^{2}}{Re} \hat{\boldsymbol{u}} + \left(\boldsymbol{I} - \frac{\boldsymbol{k}\boldsymbol{k}}{k^{2}}\right) \frac{\boldsymbol{M}}{1 + \boldsymbol{M}} \mathbf{1}_{g} \hat{\boldsymbol{n}}.$$
(2.19)

Applying the method of characteristics, the conservation equations can be converted to ordinary differential equations (ODEs) with respect to time along the characteristics defined by

$$\frac{\mathrm{d}\boldsymbol{k}}{\mathrm{d}t} = -\nabla \boldsymbol{u}_b \cdot \boldsymbol{k}.\tag{2.20}$$

The conservation equations along the characteristics with a turning wavevector given by (2.20) are

$$\frac{\mathrm{d}\hat{n}}{\mathrm{d}t} + \mathrm{i}\mathbf{1}_{g} \cdot \boldsymbol{k}\hat{n} = \mathrm{i}2\nabla\boldsymbol{u}_{b} : \boldsymbol{k}\hat{\boldsymbol{u}} \tag{2.21}$$

$$\frac{\mathrm{d}\hat{\boldsymbol{u}}}{\mathrm{d}t} = -\left(\boldsymbol{I} - 2\frac{\boldsymbol{k}\boldsymbol{k}}{k^{2}}\right)\nabla\boldsymbol{u}_{b}^{\mathrm{T}} \cdot \hat{\boldsymbol{u}} - \mathrm{i}\frac{\boldsymbol{M}}{1+\boldsymbol{M}}\mathbf{1}_{g} \cdot \boldsymbol{k}\hat{\boldsymbol{u}} - \frac{1}{1+\boldsymbol{M}}\frac{k^{2}}{Re}\hat{\boldsymbol{u}} + \left(\boldsymbol{I} - \frac{\boldsymbol{k}\boldsymbol{k}}{k^{2}}\right)\frac{\boldsymbol{M}}{1+\boldsymbol{M}}\mathbf{1}_{g}\hat{\boldsymbol{n}}.$$
(2.22)

The condition (2.20) reflects the fact that a wave of arbitrary initial orientation rotates under the action of the shearing and its wavelength evolves as the wave is stretched and compressed by the straining component of the imposed flow. As a result of the turning wavevector, these plane-wave disturbances exhibit a non-separable dependence on space and time. A classical approach in stability analysis is to write the disturbance equations in the form

$$\frac{\mathrm{d}x}{\mathrm{d}t} = Ax\tag{2.23}$$

where x is a multidimensional vector that represents the unknowns of the problem and A is an operator that contains the governing equations. When A is constant in time, the solution to (2.23) is

$$\mathbf{x}(t) = \exp(t\mathbf{A})\mathbf{x}(t=0). \tag{2.24}$$

The usual procedure is then to analyse the spectrum of the operator A. However, this method fails in the case we are considering, because A is now time dependent. Integrating (2.23) becomes challenging both conceptually and numerically. Dyson (1949) has proposed a formal solution that makes use of a time-ordering operator \mathcal{T}

$$\mathbf{x}(t) = \mathcal{T}\left\{\exp\left(\int_0^t \mathbf{A}(\tau)d\tau\right)\right\}\mathbf{x}(t=0)$$
 (2.25)

that is not practical for computational purposes. A numerically tractable expansion found in Bellman (1997)

$$\mathbf{x}(t) = \lim_{n \to \infty} \left\{ \mathbf{I} + \int_0^t dt_n \int_0^{t_n} dt_{n-1} \dots \int_0^{t_1} dt_0 \mathbf{A}(t_0) \mathbf{A}(t_1) \dots \mathbf{A}(t_n) \right\} \mathbf{x}(t = 0)$$
 (2.26)

was used by Schmid & Kytomaa (1994) in the context of granular flow in unbounded homogeneous shear. Alternatively, the method of Magnus (1954) provides a representation based on an exponential of a series of operators. The common denominator to these different approaches, is the high degree of complexity of the form of solution and the difficulty of implementation. In contrast, we shall demonstrate, in our case, that for the large wavenumbers, which give the largest perturbation growth, one can obtain simpler analytical approximate solutions to the (2.21) and (2.22) using the WKB method.

In the following, we will investigate the particular case in which gravity is aligned with the velocity gradient of the imposed shear flow, so that $\mathbf{1}_g = -e_2$ and $\nabla u_b = e_2 e_1$. In this configuration, the number density equation (2.21) is

$$\frac{\mathrm{d}\hat{n}}{\mathrm{d}t} = \mathrm{i}k_2\hat{n} + \mathrm{i}2k_1\hat{u}_2 \tag{2.27}$$

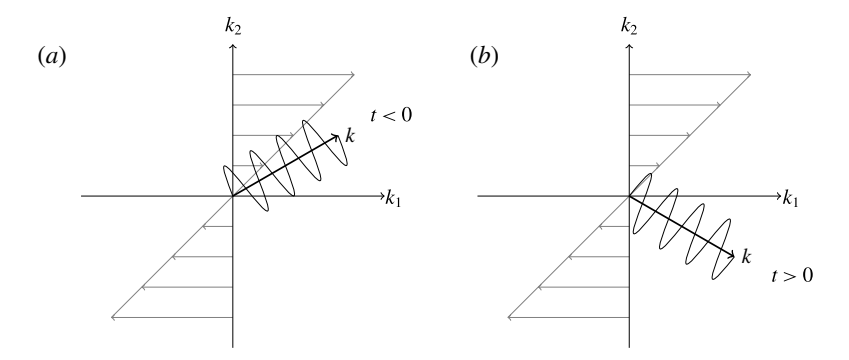


FIGURE 1. As the wave rotates, it goes from an upstream configuration corresponding to negative times, to a downstream configuration corresponding to positive times: (a) upstream configuration; (b) downstream configuration.

and the momentum equation (2.22) along the e_2 axis is

$$\frac{\mathrm{d}\hat{u}_2}{\mathrm{d}t} = 2\frac{k_2k_1}{k^2}\hat{u}_2 + \frac{M}{1+M}ik_2\hat{u}_2 - \frac{M}{1+M}\left(1 - \frac{k_2^2}{k^2}\right)\hat{n} - \frac{1}{1+M}\frac{k^2}{Re}\hat{u}_2. \tag{2.28}$$

The velocity component along e_1 , that is \hat{u}_1 , can be easily obtained with the continuity equation. From the relation (2.20), the two components of the wavevector along directions e_1 and e_3 have constant values, while along e_2 the component is $k_2 = -k_1 t$ where we choose the origin of time such that k_2 becomes zero at t=0. Thus, for negative values of time, the wavevector is pointing upstream ($k_2 > 0$) while, for positive values of time, it is pointing downstream ($k_2 < 0$) as illustrated in figure 1. We will consider initial times t_0 that may be positive or negative according to the desired initial orientation of the wavevector. We constrain the analysis to perturbations for which $k_3 = 0$. The 3-component of the wavenumber makes no qualitative difference in the dynamics of the system.

2.3. Numerical investigation

To understand the dynamics of coupled particle number density and fluid momentum perturbations in a sheared gas-solid suspension we begin by examining numerical solutions to (2.27) and (2.28) for the inviscid case $Re \to \infty$ with a moderate mass loading M = 0.5. Figure 2 illustrates the response of the number density perturbation and the vertical component of the fluid velocity perturbation to an initial disturbance of the fluid momentum scaled with an arbitrary small amplitude ϵ of $(\hat{n} = 0, \hat{u}_2 = 1)$. Note that since the initial scaled amplitude is unity, the later scaled amplitude is also equal to the relative amplification of the wave. A comparison of figure 2(a,b) with (c,d) illustrates the effect of increasing the wavenumber of the perturbation, while a comparison of figure 2(c,d) with (e,f) indicates the effect of changing from an initially upstream to downstream wavevector orientation. We can see in figure 2(d)that the momentum disturbance for an upstream wavevector grows significantly in amplitude as the wavevector approaches a horizontal orientation and decays with time thereafter. This behaviour is qualitatively similar to that observed in Kelvin waves in a single-phase fluid although the transient growth is stronger in the presence of inertial particles. The number density perturbation (figure 2c) remains small

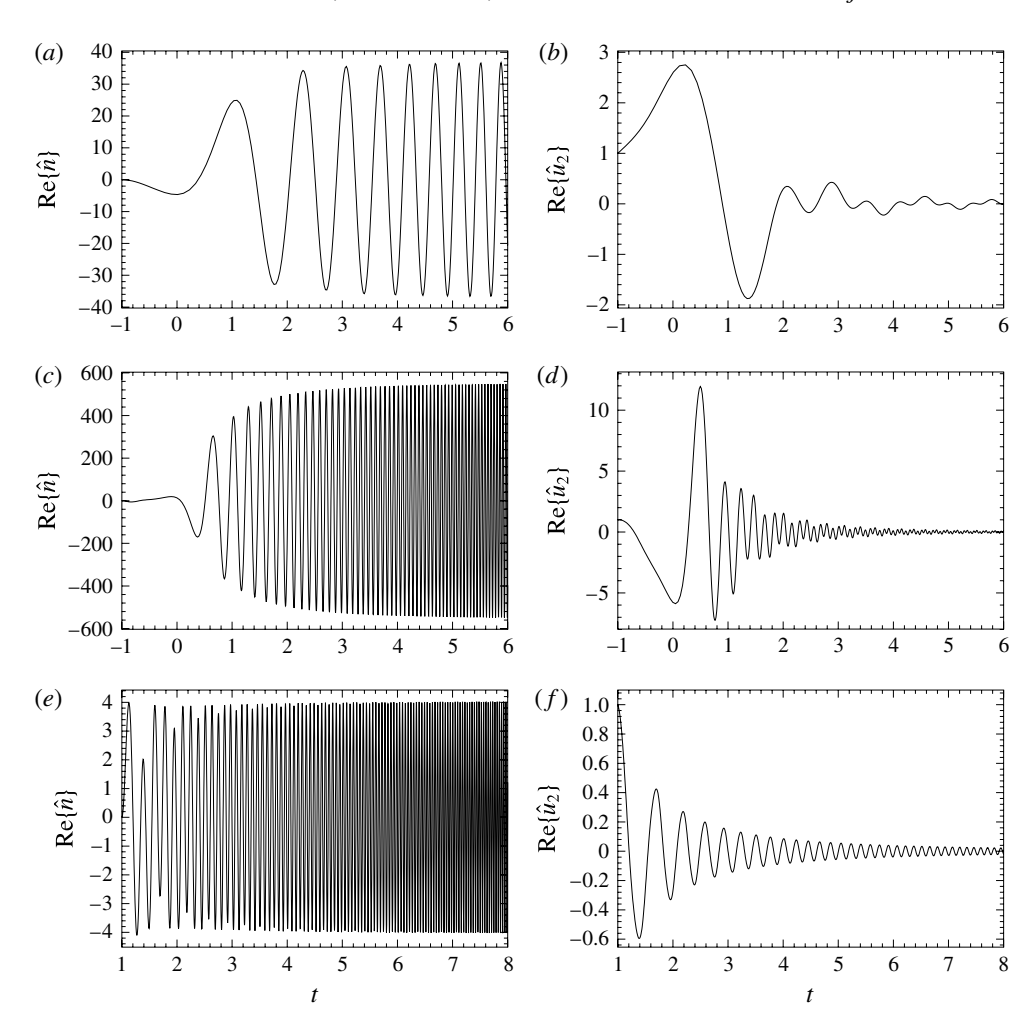


FIGURE 2. Real part of the number density and vertical fluid velocity for the initial conditions $\hat{n}=0$, $\hat{u}_2=1$: (a) \hat{n} , $k_1=k_2(t_0)=3$; (b) \hat{u}_2 , $k_1=k_2(t_0)=3$; (c) \hat{n} , $k_1=k_2(t_0)=20$; (d) \hat{u}_2 , $k_1=k_2(t_0)=20$; (e) \hat{n} , $k_1=20$, $k_2(t_0)=-20$; (f) \hat{u}_2 , $k_1=20$, $k_2(t_0)=-20$. Different orientations and magnitudes of the wavevector are considered. The initial time is t_0 . The Reynolds number is taken to be infinitely large and the mass loading is M=0.5.

while the wavevector is upstream of the horizontal orientation and grows rapidly as the wavevector passes downstream of horizontal eventually saturating with an amplification of about 500. While this behaviour does not represent an exponential growth of a small perturbation as can occur in a linearly unstable unsheared system, growth by more than two orders of magnitude can potentially lead to nonlinear effects or secondary instabilities for a relatively modest finite amplitude of the initial disturbance.

Comparing figure 2(a,b) with (c,d), we see that increasing the wavenumber of the perturbation increases both the amplitude and frequency of the resulting number density and momentum perturbations. This suggests that high-wavenumber perturbations are most amplified at least in the inviscid limit. Assuming that a nonlinear mechanism exists by which number density perturbations can create

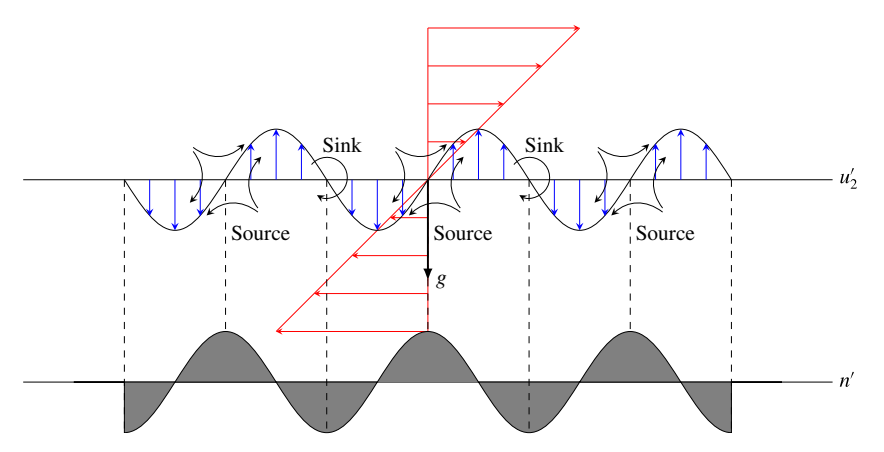


FIGURE 3. (Colour online) Mechanism of instability of a particle laden simple shear flow: a disturbance to the fluid flow (arrows) leads through preferential concentration to variations in particle number density (grey). The particle concentration variations create a fluctuating gravitational force which enhances the fluid velocity disturbance.

sustained momentum perturbations this observation would be consistent with the observation of Elghobashi & Truesdell (1993) that turbulence enhancement by settling particles is most pronounced at high wavenumbers. The number density perturbations in figure 2(c) oscillate with a high frequency while changing amplitude at a slower rate, indicating that the dynamics are represented by multiple time scales in the limit $k_1 \gg 1$. An examination of the behaviour at different wavenumbers indicates that the oscillations for values of t not too close to zero occur with a period of order $1/k_1$, while the amplitude varies over an O(1) time scale. The period of the oscillations grows at $t \to 0$ and the period and time scale of amplitude variation are of the same order as t when $t = O(k_1^{1/2})$. These observations suggest that a multiple time scale asymptotic analysis is applicable for $k_1 \gg 1$, the limit in which the largest growth of the perturbation is observed. The behaviour near t = 0 does not show a distinctive time scale separation, something that is indicative of a so-called turning point, a point in time around which the different time scales collapse into one. These findings motivate the use of the WKB asymptotic method, a method that addresses the separate time scales and connects them through the turning point.

Further evidence of the importance of the turning point at t = 0 can be seen by comparing the response to an initially upstream wave $(k_2(t_0) > 0)$ in figure 2(c,d) and an initially downstream wave $(k_2(t_0) < 0)$ in figure 2(e,f). While a substantial growth of the disturbance occurs for an upstream wave, the downstream wave exhibits no growth of the number density disturbance and a monotonic decay in the amplitude of the momentum disturbance. From this comparison, we see that the turning point at t = 0 plays a crucial role in creating a large growth of the disturbance.

The mechanism of the instability is illustrated in figure 3. The divergence of the particle velocity field, which results in preferential concentration of particles, is proportional to the difference between the mean-squared strain rate and rotation rate (2.20). The base state simple shear flow has equal portions of strain and rotation and results in no preferential concentration. However, a sinusoidally varying fluid velocity perturbation alternately reinforces and attenuates the vorticity due to the imposed flow leading to regions where the number density is decreased and increased. This



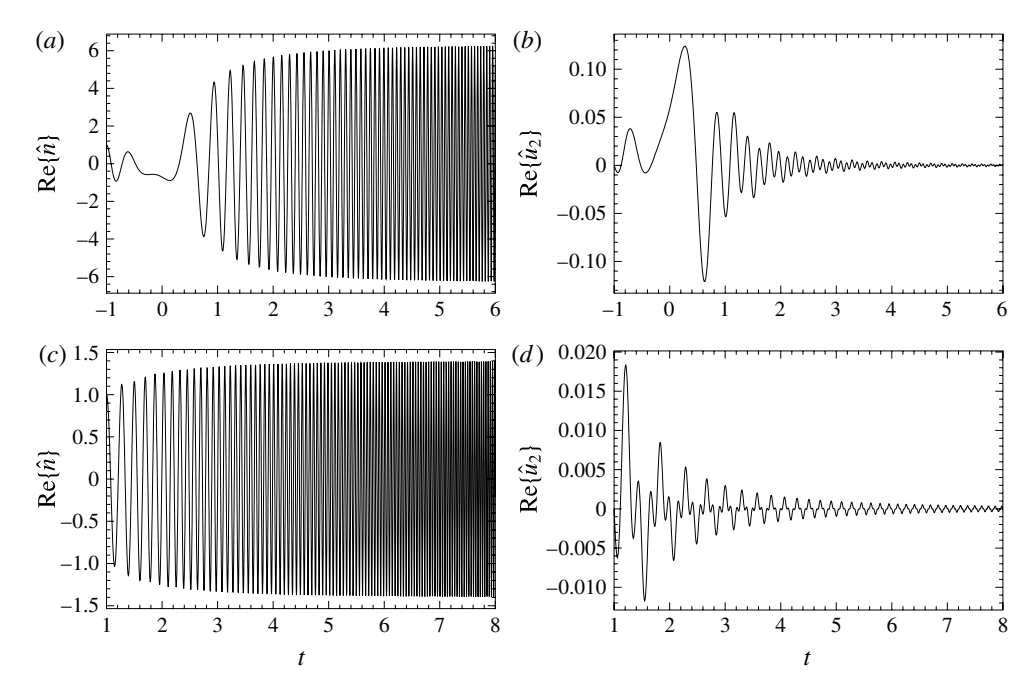


FIGURE 4. Real part of the number density and vertical fluid velocity for the initial conditions $\hat{n}=1$, $\hat{u}_2=0$: (a) \hat{n} , $k_1=k_2(t_0)=20$; (b) \hat{u}_2 , $k_1=k_2(t_0)=20$; (c) \hat{n} , $k_1=20$, $k_2(t_0)=-20$; (d) \hat{u}_2 , $k_1=20$, $k_2(t_0)=-20$. Different orientations and magnitudes of the wavevector are considered. The initial time is t_0 . The Reynolds number is taken to be infinitely large and the mass loading is M=0.5

number density wave illustrated in grey in the figure is directly out of phase with the momentum disturbance. Nonetheless, the gravity force acting on the perturbed number density field (third term in the right-hand side of (2.28)) can reinforce the momentum wave if the two waves propagate relative to one another. This propagation does occur and is facilitated by the particles' inertia, the transient effects due to the shear-induced rotation of the wave and the sedimentation of the particles relative to the wave when the wavevector is not horizontal.

Now, consider an initial number density perturbation $(\hat{n}=1, \hat{u}_2=0)$. The simulations reported in figure 4 show the same features at high k_1 (time scale separation, sharp transient at t=0) as for a momentum perturbation. The final number density disturbance is again larger when the initial disturbance has a larger wavenumber. However, amplification of the number density disturbance created by an initial disturbance to the fluid velocity (figure 2c) is much larger than that due to an initial number density disturbance (figure 4a).

Figure 5 illustrates the effect that mass loading has on the growth in amplitude of the number density and fluid velocity due to an initial momentum disturbance (a,b) and an initial number density disturbance (c,d). It can be seen that the saturation amplitude of the number density wave and the transient peak of the fluid velocity disturbance both grow significantly with increasing mass loading and this growth occurs for both initial number density and momentum disturbances.

The inviscid numerics indicate that the largest growth in the amplitude of disturbances occurs at the highest dimensionless wavenumbers, making the inviscid

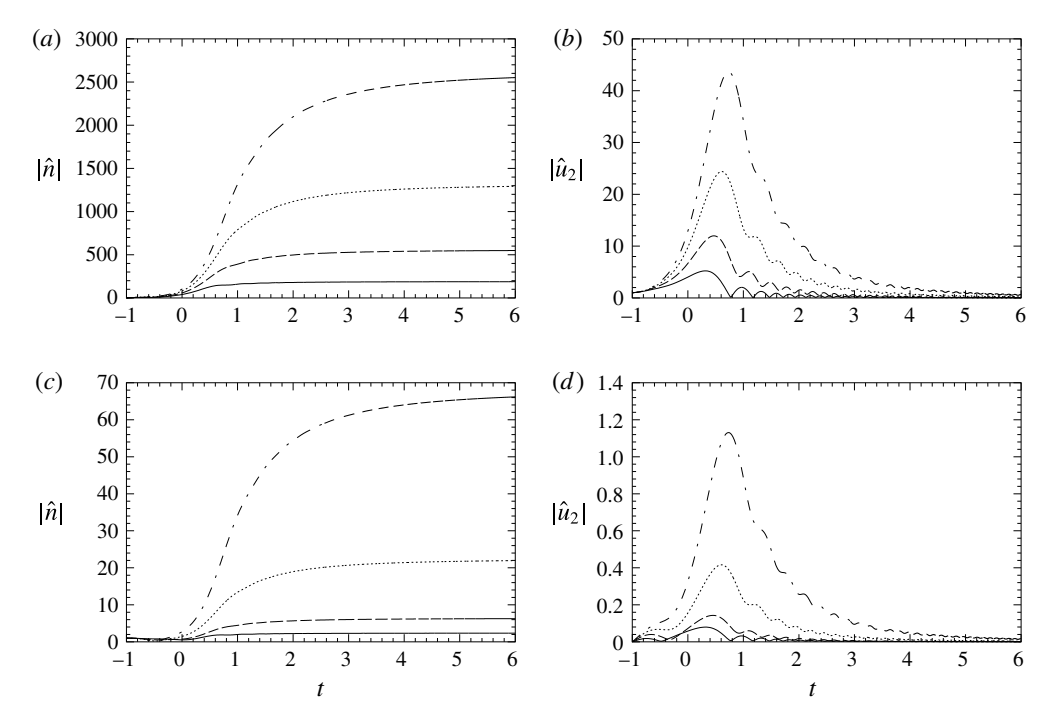


FIGURE 5. Amplitude of the number density and the vertical fluid velocity due to a momentum disturbance $\hat{n} = 0$, $\hat{u}_2 = 1$ (a,b) and a number density disturbance $\hat{n} = 0$, $\hat{u}_2 = 1$ (c,d) for an inviscid flow with $k_1 = k_2(t_0) = 20$. The mass loading is M = 0.25 (----), 0.75 (···-), 1 (----).

analysis ill-posed. However, it may be expected that viscous effects will reduce the growth rate when the dimensional wavelength becomes smaller than $\sqrt{\nu/\Gamma}$ the distance over which viscous diffusion can damp fluid velocity variations during the $O(1/\Gamma)$ time required for shear-induced rotation of the wave. We will see that this leads to a finite growth rate at an intermediate wavenumber in the well-posed viscous problem.

The effect of finite Reynolds number on an initial momentum perturbation with $k_1 = 20$ is illustrated in figure 6, where the Reynolds number is varied from 10 000 to 1000, 500 and 100. The $Re = 10\,000$ results in figure 6(a,b) are very close to the corresponding inviscid results in figure 2(c,d). In the range Re = 1000-500, the saturation amplitude of the number density wave begins to decreases and by Re = 100 it is reduced over 50-fold compared with the inviscid result. These results indicate that the large amplification of the disturbance that was seen in the inviscid numeric can be retained at large but finite Reynolds numbers.

We have suggested based on the inviscid numeric that an asymptotic analysis based on $k_1 \gg 1$ would be fruitful since the instability is most amplified in this limit. One might raise the concern, however, that viscous effects become increasingly important at higher wavenumber and might make high-wavenumber disturbances less amplified in viscous gases. To explore this issue, we plot the saturation amplitude of the number density wave due to an initial upstream momentum disturbance as a function of wavenumber in figure 7 for two viscous cases with Re = 1500 and Re = 2500. At moderate values of the wavenumber, the saturation amplitude grows

Downloaded from https://www.cambridge.org/core. Cornell University Library, on 30 May 2017 at 14:48:00, subject to the Cambridge Core terms of use, available at https://www.cambridge.org/core/terms. https://doi.org/10.1017/jfm.2015.136

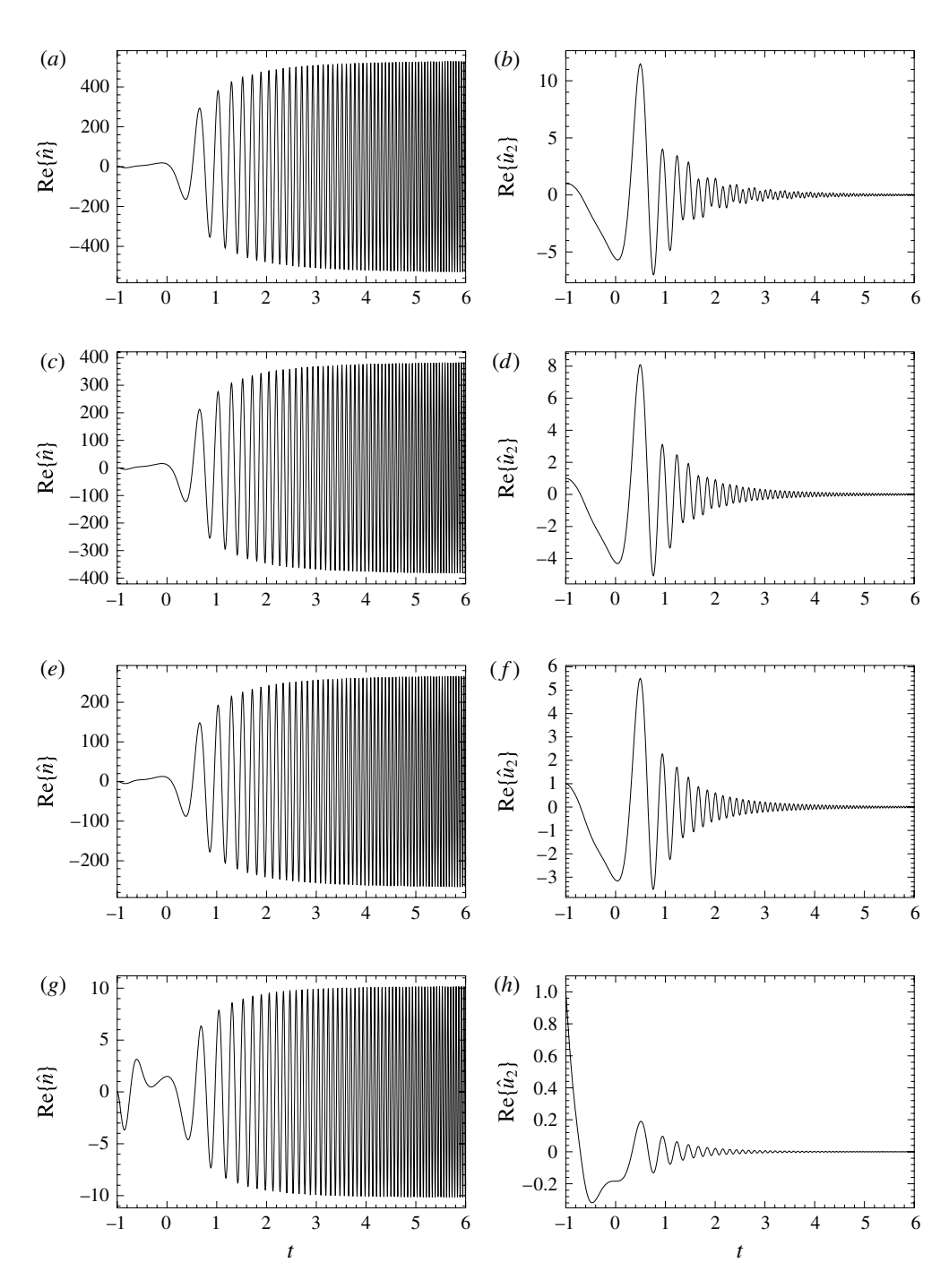


FIGURE 6. Number density and vertical fluid velocity for $Re = 10\,000,\ 1000,\ 500$ and 100: (a) \hat{n} , $Re = 10\,000$; (b) \hat{u}_2 , $Re = 10\,000$; (c) \hat{n} , Re = 1000; (d) \hat{u}_2 , Re = 1000; (e) \hat{n} , Re = 500; (f) \hat{u}_2 , Re = 500; (g) \hat{n} , Re = 100; (h) \hat{u}_2 , Re = 100. The initial conditions are a momentum perturbation and a wavevector such that $k_1 = k_2(t_0) = 20$. The mass loading is M = 0.5.

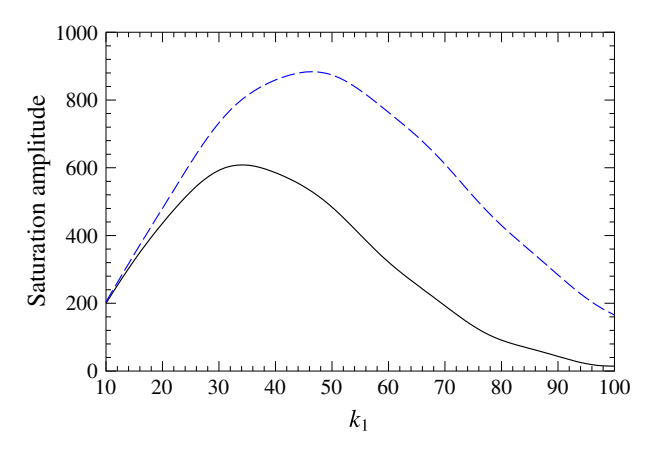


FIGURE 7. (Colour online) Saturation amplitude generated by a momentum perturbation at $t_0 = -1$ for a mass loading M = 0.5. The solid curve corresponds to Re = 1500 and the dashed curve to Re = 2500.

with amplitude similarly to the inviscid simulations. The amplitude then passes through a maximum and decreases at high wavenumbers. The optimal wavenumber is $k_1 \approx 35$ and $k_1 \approx 50$ at Re = 1500 and Re = 2500, respectively, and further analysis shows that the optimum wavenumber scales as $k_1 \sim Re^{1/2}$. The dimensional wavelength of the optimum perturbation is $(\nu/\Gamma)^{1/2}$. As one might expect, this is the wavelength at which viscous diffusion of momentum can propagate across the wavelength attenuating the momentum disturbance within the time it takes the wave to turn toward the horizontal and amplify. Smaller wavelength disturbances are damped by viscous diffusion while larger wavelengths experience less amplification as indicated by the inviscid numerics.

We have seen that the optimum wavenumber remains asymptotically large in a viscous fluid when the Reynolds number is asymptotically large. With this observation in mind, we will employ a WKB asymptotic analysis for $k_1 \gg 1$ to obtain more insight and analytical predictions for the growth of the disturbances, exploring the inviscid case in § 3 and the viscous case in § 4.

3. Asymptotic analysis for large wavenumber using WKB method: inviscid analysis

3.1. Outer region

In this section, we apply a WKB multiple time scale asymptotic analysis valid for $k_1\gg 1$ to the inviscid equations for the velocity and number density fluctuations. An in-depth explanation of the WKB method (sometimes referred to as WKBJ after Wentzel-Kramer-Brillouin-Jeffreys) has been provided in Hinch (1991) and Bender & Orszag (1999). The WKB approach is often used for analysing the behaviour of a wave in an inhomogeneous medium (or a potential barrier) with properties that might undergo a sharp transition. This transition layer would then connect the wave properties on either side. In the present context, the analysis we present is adapted for turning waves with a wavevector that varies with time. One might consider then that the velocity and number density perturbations experience varying effects of gravity, preferential concentration and particle inertia as they rotate and dilate.

It is most convenient to perform the WKB method on a single ODE obtained by combining (2.27) and (2.28) as

$$\frac{\mathrm{d}^2 \hat{n}}{\mathrm{d}t^2} + A(t)\frac{\mathrm{d}\hat{n}}{\mathrm{d}t} + B(t)\hat{n} = 0. \tag{3.1}$$

Making use of $k_2 = -k_1t$ and dropping viscous terms, we can express the two coefficient functions A and B as

$$A(t) = k_1 \left(i \frac{1 + 2M}{1 + M} t + \frac{1}{k_1} \frac{2t}{1 + t^2} \right)$$

$$= k_1 \left(a_0(t) + \frac{1}{k_1} a_1(t) \right)$$

$$B(t) = i k_1^2 \left(i \frac{M}{1 + M} t^2 + \frac{1}{k_1} \left(\frac{2}{1 + M} \frac{t^2}{1 + t^2} + \frac{1 + 3M}{1 + M} \right) \right)$$

$$= k_1^2 \left(b_0(t) + \frac{1}{k_1} b_1(t) \right).$$
(3.2)

We begin by developing approximate solutions to (3.1) with (3.2) and (3.3) valid for times that are not close to zero, i.e. times at which the wavevector is either significantly upstream (t < 0) or downstream (t > 0) of the horizontal orientation. From the numerical solution in figure 2(c), we expect that the number density field oscillates with an $O(k_1)$ frequency and that the frequency and amplitude of the wave vary over O(1) time scales. The standard form of the solution sought by the WKB method involves an exponential of an expansion in k_1 of the form:

$$\hat{n}(t) = \exp\left(k_1 \sum_{n=0}^{\infty} \left(\frac{1}{k_1}\right)^n S_n(t)\right)$$
(3.4)

where the first term with an imaginary $S_0(t)$ provides the $O(k_1)$ frequency that varies over O(1) time periods and S_1 provides a modulation of the amplitude over O(1) time scales. It is generally expected that this form will provide an accurate representation of the solution for most times outside a short interval around a point in time referred to as a turning point. The exponential form is valid as long as $(1/k^n)$ $S_n \ll (1/k^{n+1})S_{n+1}$ is satisfied. It can be seen from (3.3) that this outer solution will break down when $b_0(t) \sim b_1(t)/k_1$, corresponding to times $t \sim 1/\sqrt{k_1}$. An inner solution valid for such small times when the wavevector is nearly horizontal will be developed later. Substituting this expansion in the number density equation yields a series of ODEs:

$$O(k_{1}) S_{0}^{\prime 2} + a_{0}S_{0}^{\prime} + b_{0} = 0$$

$$O(1) (2S_{0}^{\prime} + a_{0})S_{1}^{\prime} + S_{0}^{\prime\prime} + a_{1}S_{0}^{\prime} + b_{1} = 0$$

$$O\left(\frac{1}{k_{1}^{n-1}}\right) (2S_{0}^{\prime} + a_{0})S_{n}^{\prime} + S_{n-1}^{\prime\prime} + \sum_{j=1}^{n-1} S_{j}^{\prime}S_{n-j}^{\prime} + a_{1}S_{n-1}^{\prime} = 0 \text{for all } n \geqslant 2.$$

$$(3.5)$$

The order $O(k_1)$ equation is a quadratic equation for S'_0 and yields a pair of solutions:

$$S_0' = \frac{-a_0 \pm (a_0^2 - 4b_0)^{1/2}}{2}. (3.6)$$

101

Each of the higher- (nth)-order equations provides a linear equation for S'_n in terms of known results from the previous orders. In particular, the first order solution is

$$S'_{1} = -\frac{S''_{0} + b_{1} + a_{1}S'_{0}}{2S'_{0} + a_{0}}$$
(3.7)

giving one solution for each of the solutions for S_0 . As in most applications of the WKB method, zeroth- and first-order terms in the expansion provide an adequate approximation of the outer solutions by specifying the time-varying frequency and amplitude, respectively. To understand the physical nature of the two solutions, it is useful to express a_0 and b_0 as functions of terms appearing in the conservation equations:

$$a_0 = \frac{1}{k_1} \left(\frac{M}{1+M} \frac{FT[\mathbf{1}_g \cdot \nabla u_2]}{FT[u_2]} + \frac{FT[\mathbf{1}_g \cdot \nabla n]}{FT[n]} \right)$$
(3.8)

$$b_0 = \frac{1}{k_1^2} \frac{M}{1+M} \frac{FT[\mathbf{1}_g \cdot \nabla u_2]}{FT[u_2]} \frac{FT[\mathbf{1}_g \cdot \nabla n]}{FT[n]}$$
(3.9)

where FT denotes the Fourier transform operator. The two solution for the zeroth order are

$$k_1 S_0^{M} = \int_0^t \frac{M}{1+M} \frac{FT[\mathbf{1}_g \cdot \nabla u_2]}{FT[u_2]} dt' = -i \frac{M}{1+M} k_1 \frac{t^2}{2}$$
 (3.10)

$$k_1 S_0^{N} = \int_0^t \frac{FT[\mathbf{1}_g \cdot \nabla n]}{FT[n]} dt' = -ik_1 \frac{t^2}{2}.$$
 (3.11)

We will refer to S_0^N as the number density mode (or N mode) since its frequency arises from the rate of convection of particle number density by sedimentation as it appears in the number density conservation equation. Here S_0^M will be called the momentum mode (M mode), because its frequency arises from the convection of momentum by particle sedimentation as it appears in the momentum conservation equation. The propagation of momentum differs from the settling speed by a factor of M/(1+M) because momentum is transported only by the particles (M) but is stored by both particle and gas (1+M). The reader is referred to § 3.2 for further explanations of this choice of nomenclature.

The amplitudes of the modes are determined by S_1^{M} and S_1^{N} and (3.7) which governs these quantities can be written as

$$S_1' = -\frac{a_1}{2} - \frac{1}{4} \frac{u'}{u} \pm \frac{1}{2} \frac{a_0' + a_1 a_0 - 2b_1}{u^{1/2}}$$
(3.12)

where $u = a_0^2 - 4b_0$. We can integrate the equation to find the first-order term:

$$S_1^{M}(t) = -(1+2M)\ln(|t|) - (1-M)\ln(1+t^2)$$
(3.13)

$$S_1^{N}(t) = 2M \ln(|t|) - M \ln(1 + t^2).$$
 (3.14)

Therefore, the two modes are

$$\hat{n}^{M}(t) = \frac{1}{|t|^{1+2M}} \frac{1}{(1+t^{2})^{1-M}} \exp\left(-ik_{1} \frac{M}{1+M} \frac{t^{2}}{2}\right)$$
(3.15)

$$\hat{n}^{\mathbb{N}}(t) = \left(\frac{t^2}{1+t^2}\right)^M \exp\left(-\mathrm{i}k_1\frac{t^2}{2}\right). \tag{3.16}$$

Here it becomes clear that k_1S_0 constitutes the phase, while S_1 controls the amplitude. Note that the two modes are waves with effective angular frequencies $\omega^{\mathrm{M}}(t) = (k_1/2)(M/(1+M))t$ for the momentum mode and $\omega^{\mathrm{N}}(t) = (k_1/2)t$ for the number density mode. These frequencies depend on time and increase as |t| increases and the wavevector is aligned with gravity. The increase in frequency with |t| is readily apparent in figure 2(c,d) and it results from the fact that the wavelength of the disturbance decreases as 1/t as $|t| \to \infty$ so that the time required for particles or momentum to traverse the wave decreases. It is interesting to note that the amplitude of the momentum mode grows when the wavevector is upstream of the horizontal (t < 0) and decays with time downstream (t > 0). This behaviour might be expected as the case M=0 corresponding to a single-phase fluid recovers Kelvin modes, which are known to undergo transient amplification. In contrast the number density mode decreases in amplitude for t < 0 and grows for t > 0. It will be seen that the turning point near t=0 allows a transformation of disturbance amplitude between the two modes. Thus, an upstream momentum mode that triggers a downstream number density mode can be expected to lead to the largest growth of perturbations.

To obtain more insight into the nature of the modes it is useful to consider their fluid velocity disturbances, which can be obtained from (2.27) as

$$\hat{u}_{2}^{\text{M}}(t) = \left(\frac{1}{2} \frac{t}{1+M} + i \frac{1}{2k_{1}} \left[\frac{1+2M}{t} + (1-M) \frac{2t}{1+t^{2}} \right] \right) \hat{n}^{\text{M}}(t)$$
(3.17)

$$\hat{u}_{2}^{N}(t) = -i\frac{M}{k_{1}} \left(\frac{1}{t} - \frac{t}{1+t^{2}} \right) \hat{n}^{N}(t). \tag{3.18}$$

As suggested by its name, the number density mode has a fluid velocity that is $O(1/k_1)$ smaller than its number density. The momentum mode has comparable fluid velocity and number density disturbances.

The general solution is a linear combination of the two modes

$$\hat{n}(t) = \Lambda_{\mathsf{M}} \hat{n}^{\mathsf{M}}(t) + \Lambda_{\mathsf{N}} \hat{n}^{\mathsf{N}}(t) \tag{3.19}$$

$$\hat{u}_2(t) = \Lambda_{\mathrm{M}} \hat{u}_2^{\mathrm{M}}(t) + \Lambda_{\mathrm{N}} \hat{u}_2^{\mathrm{N}}(t) \tag{3.20}$$

in which the coefficients $\Lambda_{\rm M}$ and $\Lambda_{\rm N}$ depend on the choice of initial conditions. For a fluid velocity perturbation with no initial number density disturbance, one obtains a momentum and a number density mode with comparable magnitudes $\Lambda_{\rm M} \sim \Lambda_{\rm N}$. However, the subsequent fluid velocity field is produced primarily by the momentum mode since $\hat{u}_2^{\rm N} \ll \hat{u}_2^{\rm M}$. An initial perturbation to the number density field produces primarily a number density mode with a much smaller momentum mode $\Lambda_{\rm M} \sim \Lambda_{\rm N}/k_1$. These observations along with our previous discussion of the temporal dynamics of the modes help to explain why the fluid velocity disturbances in figure 2(c,d) produced much larger growth than the number density disturbances in figure 4(a,b). The velocity initial condition produces an O(1) momentum mode that grows up to the turning point and then induces a number density mode that grows downstream of the turning point. On the other hand, the number density initial condition primarily induces a number density mode whose amplitude declines in the upstream orientations and a much smaller momentum mode that grows in the upstream region.

3.2. Mechanisms leading to time variation of the amplitudes of the modes in the outer region

In the previous discussion, we solved systematically for S_0 and S_1 in the exponential ansatz and obtained the N and M modes, two waves with effective angular frequencies $\omega^{\text{M}}(t) = (k_1/2)(M/(1+M))t$ and $\omega^{\text{N}}(t) = (k_1/2)t$ and respective amplitudes $(\tilde{u}_2^{\text{N}}, \tilde{n}^{\text{N}})$ and $(\tilde{u}_2^{\text{M}}, \tilde{n}^{\text{M}})$. Thus, for example, the number density and fluid velocity in the number density mode can be written in terms of the frequency and amplitudes as

$$\hat{n}^{N}(t) = \tilde{n}^{N} \exp(i\omega^{N}(t)t)$$

$$= \left(\frac{t^{2}}{1+t^{2}}\right)^{M} \exp\left(-ik_{1}\frac{t^{2}}{2}\right)$$
(3.21)

$$\hat{u}_2^{\mathbb{N}}(t) = \tilde{u}_2^{\mathbb{N}} \exp(\mathrm{i}\omega^{\mathbb{N}}(t)t)$$

$$= -\mathrm{i}\frac{M}{k_1} \left(\frac{1}{t} - \frac{t}{1+t^2}\right) \hat{n}^{\mathbb{N}}(t). \tag{3.22}$$

Substituting $\hat{n}^{\mathbb{N}}(t) = \tilde{n}^{\mathbb{N}} \exp(i\omega^{\mathbb{N}}(t)t)$ and $\hat{u}_{2}^{\mathbb{N}}(t) = \tilde{u}_{2}^{\mathbb{N}} \exp(i\omega^{\mathbb{N}}(t)t)$ into (2.27) and (2.28), yields the following equations for the time variation of the amplitudes for the \mathbb{N} mode:

$$\frac{\mathrm{d}\tilde{n}^{\mathrm{N}}}{\mathrm{d}t} = 2\mathrm{i}k_{1}\tilde{u}_{2}^{\mathrm{N}} \tag{3.23}$$

$$\frac{\mathrm{d}\tilde{u}_{2}^{\mathrm{N}}}{\mathrm{d}t} = -\frac{\mathrm{i}k_{2}}{1+M}\tilde{u}_{2}^{\mathrm{N}} + \frac{2k_{2}k_{1}}{k^{2}}\tilde{u}_{2}^{\mathrm{N}} - \frac{M}{1+M}\frac{k_{1}^{2}}{k^{2}}\tilde{n}^{\mathrm{N}}.$$
(3.24)

Thus, in a reference frame of a wave that rotates with the shear flow and translates with the settling velocity, the amplitude of the number density in (3.23) changes solely due to preferential concentration. The three terms on the right-hand side of (3.24) indicate that the velocity evolves due to the propagation of momentum by settling, a shear-induced amplification upstream and diminution downstream of the horizontal orientation, and the gravitational forcing by the particles, respectively. Recalling that the fluid velocity associated with the N mode is $O(1/k_1)$ smaller than the number density, i.e. $\tilde{u}_2^N \sim \tilde{n}^N/k_1$, the leading-order solution of (3.24) involves a quasi-steady balance of the production of momentum due to the gravitational forcing and its transport by settling induced momentum flux, i.e.

$$\frac{\mathrm{i}k_2}{1+M}\tilde{u}_2^{\mathrm{N}} = -\frac{M}{1+M}\frac{k_1^2}{k^2}\tilde{n}^{\mathrm{N}} \tag{3.25}$$

which, when using $k_2 = -k_1 t$, becomes

$$\hat{u}_2^N = -i\frac{M}{k_1} \frac{1}{t(1+t^2)} \hat{n}^N. \tag{3.26}$$

The fluid velocity induced by the gravitational forcing decays as $1/(t(1+t^2))$ with increasing t because the smaller wavelength at large time increases the rate of momentum transport across the wave and the alignment of the wavevector toward the vertical direction reduces the portion of the gravitational forcing that drives a fluid velocity rather than a hydrostatic pressure field. Inserting the quasi-static approximation for the fluid velocity field (3.25) into the number density equation (3.23), we see that

$$t\frac{\mathrm{d}\tilde{n}^{\mathrm{N}}}{\mathrm{d}t} - \frac{2M}{1+t^{2}}\tilde{n}^{\mathrm{N}} = 0 \tag{3.27}$$

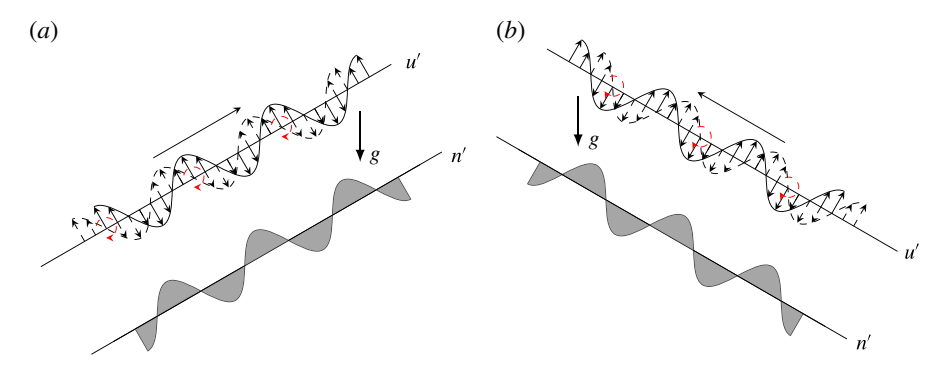


FIGURE 8. (Colour online) Mechanism leading to (a) growth of the N mode in the upstream region and (b) attenuation of the N mode in the downstream region. Waves are illustrated in the reference frame of the number density field.

$$\tilde{n}^{N} = (t^{2}/(1+t^{2}))^{M}. \tag{3.28}$$

The mechanism for the decay (in the upstream region) and growth (in the downstream region) is illustrated in figure 8. The number density field creates a wave of fluid motion that moves downward in regions of high concentration and upward in regions of low concentration (dashed lines). However, the momentum disturbance is shifted upward because the inertia of the gas causes momentum to move upward relative to the settling particles resulting in the momentum disturbance illustrated by the solid line. This momentum disturbance through preferential concentration attenuates the number density field in the upstream region and reinforces it in the downstream region.

Proceeding to analyse the M mode in a similar manner, we consider the ansatz $\hat{n}^{\text{M}}(t) = \tilde{n}^{\text{M}} \exp(i\omega^{\text{M}}(t)t)$ and $\hat{u}_{2}^{\text{M}}(t) = \tilde{u}_{2}^{\text{M}} \exp(i\omega^{\text{M}}(t)t)$ and substitute in (2.27) and (2.28),

$$\frac{\mathrm{d}\tilde{n}^{\mathsf{M}}}{\mathrm{d}t} = \frac{\mathrm{i}k_2}{1+M}\tilde{n}^{\mathsf{M}} + 2\mathrm{i}k_1\tilde{u}_2^{\mathsf{M}} \tag{3.29}$$

$$\frac{\mathrm{d}\tilde{u}_{2}^{\mathrm{M}}}{\mathrm{d}t} = 2\frac{k_{2}k_{1}}{k^{2}}\tilde{u}_{2}^{\mathrm{M}} - \frac{M}{1+M}\frac{k_{1}^{2}}{k^{2}}\tilde{n}^{\mathrm{M}}.$$
(3.30)

The M mode wave travels due to the momentum propagation caused by the settling velocity. In this reference frame, the wave at high wavenumber satisfies

$$0 = \frac{ik_2}{1+M}\tilde{n}^{M} + 2ik_1\tilde{u}_2^{M} \tag{3.31}$$

$$\frac{\mathrm{d}\tilde{u}_{2}^{\mathrm{M}}}{\mathrm{d}t} = 2\frac{k_{2}k_{1}}{k^{2}}\tilde{u}_{2}^{\mathrm{M}} - \frac{M}{1+M}\frac{k_{1}^{2}}{k^{2}}\tilde{n}^{\mathrm{M}}.$$
(3.32)

It consists of a quasi-steady number density field resulting from a balance of preferential concentration and the settling of the particles downward relative to the wave, and a momentum field whose dynamic response is driven by the convection of the base state shear flow momentum across streamlines by the disturbance (first term on the right-hand side of (3.32)) and the gravitational forcing of the particles (second term on the right-hand side). Both of these mechanisms lead to an upstream growth

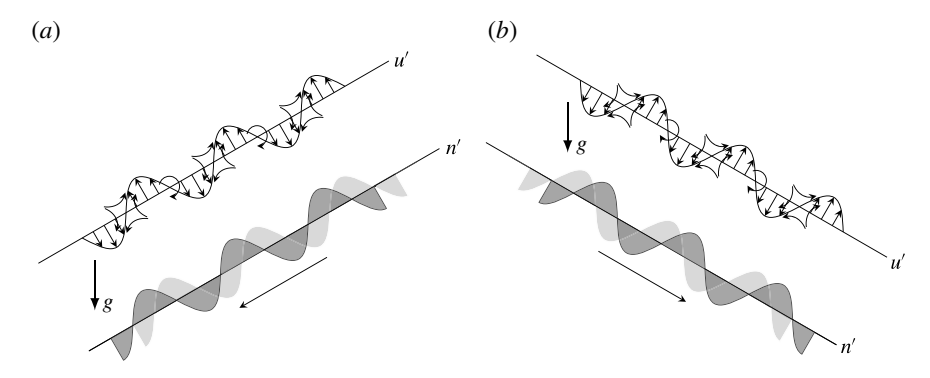


FIGURE 9. Preferential concentration mechanism for (a) the amplification of the M mode in the upstream region and (b) attenuation of the M mode in the downstream region. The waves are illustrated in the reference frame of the fluid velocity field.

and downstream decay of the amplitude of the momentum wave. The upstream growth and downstream decay due to the first term was derived by Lord Kelvin. The mechanism leading to the upstream growth and downstream decay due to the gravitational forcing is illustrated in figure 9. The fluid velocity field creates a number density field (light grey) due to preferential concentration which is shifted downward relative to the wave by sedimentation (dark grey) so that its gravitational force reinforces the wave in the upstream and attenuates it in the downstream region.

3.3. Inner region

As noted earlier, the outer solutions obtained in the previous section break down for times near t = 0 corresponding to wavevector orientations that are nearly perpendicular to the gravity and velocity gradient direction. We now seek an inner solution valid in the turning point near t = 0. To facilitate the analysis we first transform equation (3.1) into the so-called canonical form (Hinch 1991). Using the transformation

$$x(t) = \hat{n}(t) \exp\left(\frac{1}{2} \int_{-\infty}^{t} A(t') dt'\right)$$
(3.33)

the number density equation becomes

$$\frac{1}{k_1^2} \frac{\mathrm{d}^2 x}{\mathrm{d}t^2} + g(t)x = 0 \tag{3.34}$$

where

$$g(t) = \frac{1}{k_1^2} \left[B(t) - \frac{1}{2} \frac{dA}{dt}(t) - \frac{1}{4} A^2(t) \right]$$

$$= -\frac{1}{4} \left(\frac{2i\pi t}{1+M} \right)^2 + \frac{1}{k_1} \left(i\pi \frac{1+4M}{1+M} + 2i\pi \frac{1-2M}{1+M} \frac{t^2}{1+t^2} \right) - \frac{1}{k_1^2} \frac{1}{1+t^2}$$

$$= g_0(t) + \frac{1}{k_1} g_1(t) + \frac{1}{k_1^2} g_2(t). \tag{3.35}$$

This equation takes the form of a wave equation with a time-dependent frequency. The small parameter $1/k_1^2$ multiplying the highest order is a classical feature of equations necessitating a multiple time scales approach. When t = O(1), g = O(1) and the frequency is $O(k_1)$ as assumed in the outer solution. However, as $t \to 0$, $g_0 \to 0$ and the exponential expansion (3.4) breaks down when $g_0(t) \sim (1/k_1)g_1(t)$, corresponding to $t = O(1/\sqrt{k_1})$. Thus, the inner region time scale is $\tau = t\sqrt{k_1} = O(1)$. We verify that the third term can be neglected by noting that $g_0(\tau) \sim (1/k_1)g_1(\tau) = O(1/k_1)$ while $(1/k_1^2)g_2(\tau) = O(1/k_1^2)$. In terms of the inner region time scale, (3.34) becomes

$$\frac{\mathrm{d}^2 x}{\mathrm{d}\tau^2} + \left(\frac{1}{4} \frac{\tau^2}{(1+M)^2} + \mathrm{i} \frac{1+4M}{2(1+M)}\right) x = 0. \tag{3.36}$$

This equation is a parabolic cylinder equation and can be placed in a standard form by defining a time variable $T = \tau / \sqrt{2(1+M)}$, so that

$$\frac{d^2x}{dT^2} + (T^2 + \lambda)x = 0 {(3.37)}$$

where $\lambda = i(1 + 4M)$. The two solutions of this equation are parabolic cylinder functions $D_{-(1+i\lambda)/2}[\pm (1+i)T]$ as defined by Gradshteyn *et al.* (2000).

To summarise, solutions for the number density disturbance have been obtained in terms of an outer solution for the upstream wavevectors (t < 0), an inner solution for the turning point region when the wavevector is nearly horizontal $(t \to 0)$, and an outer solution for the downstream wavevector region (t > 0) and are given by

$$\hat{n}(t) = \begin{cases} \overline{\Lambda}_{N} \hat{n}^{N} + \overline{\Lambda}_{M} \hat{n}^{M} & t = O(1) \ t < 0 \\ \left\{ \Lambda_{+} D_{2M} \left[\frac{(1+i)\sqrt{k_{1}}t}{\sqrt{2(1+M)}} \right] + \Lambda_{-} D_{2M} \left[-\frac{(1+i)\sqrt{k_{1}}t}{\sqrt{2(1+M)}} \right] \right\} \\ \times \exp\left(\frac{i}{4} \frac{1+2M}{1+M} k_{1} \frac{t^{2}}{2} \right) & t = O\left(\frac{1}{\sqrt{k_{1}}} \right) \\ \underline{\Lambda}_{N} \hat{n}^{N} + \underline{\Lambda}_{M} \hat{n}^{M} & t = O(1) \ t > 0. \end{cases}$$
(3.38)

While the solutions in both outer regions, upstream and downstream, are linear combinations of M and N modes, the coefficients of the modes will differ in the two regions. For this reason, we used overlines for the pair $\{\Lambda_M, \Lambda_N\}$ in the upstream region, and underlines in the downstream region. The number density and momentum modes, \hat{n}^N and \hat{n}^M , are given by (3.15) and (3.16).

The behaviour of parabolic cylinder functions in the matching region $(|t| \gg 1/\sqrt{k_1})$, is similar to a combination of N and M modes. This makes it possible to directly match the coefficients in the upstream region with those in the downstream region, yielding

$$\underline{A}_{\mathrm{N}} = -\frac{\mathrm{i}\sqrt{\mathrm{i}}}{M\Gamma(2M)}\sqrt{\frac{\pi}{2}}\left(\frac{k_{1}}{1+M}\right)^{(1/2)+2M}\mathrm{e}^{-\mathrm{i}\pi M}\overline{A}_{\mathrm{M}} + \mathrm{e}^{-2\pi\mathrm{i}M}\overline{A}_{\mathrm{N}}$$

$$\underline{A}_{\mathrm{M}} = -\mathrm{e}^{-2\pi\mathrm{i}M}\overline{A}_{\mathrm{M}} - \mathrm{i}\sqrt{\mathrm{i}}\sqrt{\frac{2}{\pi}}2M\sin(2M\pi)\Gamma(2M)\mathrm{e}^{-\mathrm{i}\pi M}\left(\frac{1+M}{k_{1}}\right)^{(1/2)+2M}\overline{A}_{\mathrm{N}}.$$
(3.39)

The mathematical details of the matching procedure can be found in appendix A.

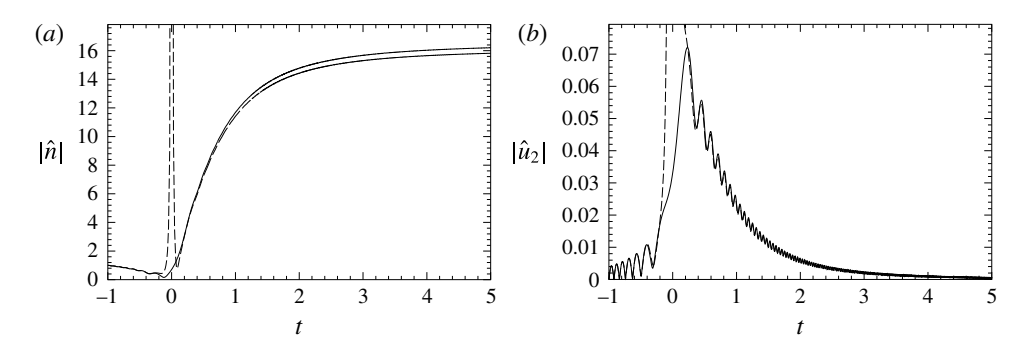


FIGURE 10. Comparison of the amplitude of number density (a) and velocity (b) predicted by numerical solution of the ODEs (solid line) and the outer WKB analytical solutions (dashed line). The initial conditions are for a number density $\hat{n}=1$, $\hat{u}_2=0$ perturbation with an initial wavevector $k_1=k_2(t_0)=125$. The Reynolds number is infinitely large and the mass loading M=0.5.

The matching provides a mixing of modes as one crosses the turning point. In fact, one can see from (3.39) that each of the upstream modes generate both N and M modes in the downstream region. A closer examination shows that an incoming N mode creates a downstream N mode whose coefficient differs from that for the upstream mode only by a phase shift as well as a momentum mode whose coefficient is smaller by a factor $k_1^{-(1/2)-2M}$ than that of the incoming N mode. The latter small contribution decays further with time for t > 0. An upstream M mode is much more effective in creating downstream disturbances. It induces a downstream M mode with a phase shift relative to the upstream mode. More importantly, it generates a downstream N mode whose coefficient is $k_1^{(1/2)+2M}$ larger than the upstream M mode coefficient. The growth of the number density and velocity disturbances does not occur primarily within the turning point since $|\overline{\Lambda}_{M}\hat{n}^{M}(t=-1/\sqrt{k_{1}})| \sim |\Lambda_{M}\hat{n}^{N}(t=1/\sqrt{k_{1}})|$. However, by transforming these disturbances from an N mode to an M mode, the disturbance is able to grow in both the upstream and downstream regions. This observation explains the previous numerical results (figures 2 and 4) that an initial condition corresponding to an upstream fluid velocity disturbance which primarily excites the M mode leads to a much larger downstream number density disturbance than is created by an initial disturbance of the number density field.

To demonstrate the validity of the WKB analysis presented above, we present in figure 10 a comparison between the WKB analytical predictions for the upstream and downstream outer regions and results obtained by numerically integrating the original ODEs. The downstream WKB results make use of the relationships (3.39) between upstream and downstream mode coefficients obtained by matching with the inner region. The oscillations in the amplitudes (more visible for the velocity), which are also reproduced by the theoretical solution, come from the interferences between the two complex modes. The figure proves the validity of the matching relations (3.39) and validates the treatment of the inner region.

To provide a succinct measure of the growth of the number density fluctuations due to an initial perturbation, we define two growth functions, G_1 corresponding to an initial number density perturbation $(\hat{n}|_{t_0} = 1 \text{ and } \hat{u}_2|_{t_0} = 0)$ and G_2 to a momentum

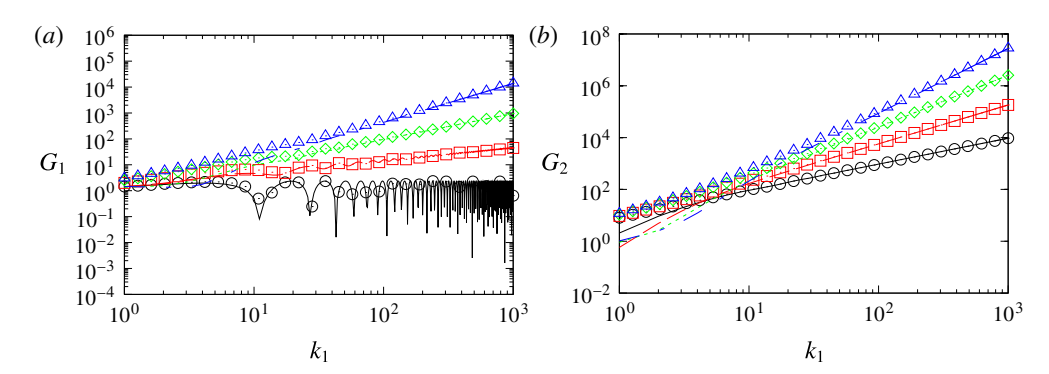


FIGURE 11. (Colour online) Amplitude growth (a) G_1 and (b) G_2 as a function of k_1 . The initial configuration is $k_2(t_0) = k_1$, i.e. $t_0 = -1$. Symbols represent simulations while lines represent theory. Four mass loadings are considered: M = 0.25 (——/ \odot), 0.5 (——/ \Box), 0.75 (···/ \diamondsuit), 1 (— · —/ \triangle).

perturbation $(\hat{n}|_{t_0} = 1 \text{ and } \hat{u}_2|_{t_0} = 0)$, in terms of the ratio

$$G_i(k_1, M, t_0) = \lim_{t \to +\infty} \frac{\|\mathbf{x}(t)\|}{\|\mathbf{x}(t_0)\|}, \quad i \in \{1, 2\}$$
(3.40)

where the vector $\mathbf{x} = (\hat{n}, \hat{u}_2)$ is a generalised representation of the solution, and $\|\mathbf{x}\| = \sqrt{\hat{n}^2 + \hat{u}_2^2}$ the 2-norm. The index *i* represents the type of initial condition considered: by definition i = 1 refers to a number density perturbation and i = 2 refers to a momentum perturbation. Note that in both cases $\|\mathbf{x}(t_0)\| = 1$, and because u_2 decays at long times, the growth functions G_1 and G_2 represent the saturation amplitude of the number density due to a unity perturbation of each of the two types, i.e.

$$G_i(k_1, M, t_0) = \lim_{t \to +\infty} |\hat{n}(t)|, \quad i \in \{1, 2\}.$$
 (3.41)

Figure 11(a) shows the growth function G_1 for different values of the mass loading M. The initial time has been set to $t_0 = -1$ which means that the wave is initiated in an upstream configuration with a 45° angle from the horizontal axis $(k_2 = k_1)$. We observe good agreement between the theory (dashed lines) and the simulations (solid lines) as we increase k_1 . The growth for M = 0.25 shows a weak dependence on k_1 . This can be explained simply by looking at the form G_1 takes using the theoretical expressions derived so far

$$G_1^{Th}(k_1, M) = \lim_{t \to \infty} |\hat{n}(t)| = |\underline{\Lambda}_{\mathbb{N}}|$$

$$= \left| e^{-2\pi i M} \overline{\Lambda}_{\mathbb{N}} - \frac{i\sqrt{i}}{M\Gamma(2M)} \sqrt{\frac{\pi}{2}} \left(\frac{k_1}{1+M} \right)^{(1/2)+2M} e^{-i\pi M} \overline{\Lambda}_{\mathbb{M}} \right|. \quad (3.42)$$

The theoretical growth G_1^{Th} is a sum (weighted by some constants) of $\overline{\Lambda}_N$ and $k_1^{(1/2)+2M}\overline{\Lambda}_M$. Now, at the initial time t_0 , which was taken to be $|t_0|\sim 1$, the modes scale as $(\hat{n}^N|_{t_0}\sim 1,\ \hat{u}_2^N|_{t_0}\sim 1/k_1)$ and $(\hat{n}^M|_{t_0}\sim 1,\ \hat{u}_2^M|_{t_0}\sim 1)$. In order to satisfy the initial conditions, $\overline{\Lambda}_N\hat{n}^N|_{t_0}+\overline{\Lambda}_M\hat{n}^M|_{t_0}=1$ and $\overline{\Lambda}_N\hat{u}_2^N|_{t_0}+\overline{\Lambda}_M\hat{u}_2^M|_{t_0}=0$ the coefficients $\overline{\Lambda}_N$ and $\overline{\Lambda}_M$ scale as $\overline{\Lambda}_N\sim 1$ and $\overline{\Lambda}_M\sim 1/k_1$. Hence, the growth is a sum of a function of order

one and a function $k_1^{(1/2)+2M}\overline{\Lambda}_M$ that varies as $k_1^{-(1/2)+2M}$, which explains the absence of dependence on k_1 for M=0.25.

In figure 11(b), we plot the evolution of the growth function G_2 as defined in the case $(\hat{n}|_{t_0} = 0, \hat{u}_2|_{t_0} = 1)$ for different values of the mass loading. Contrary to the previous case, we do not observe a plateau for M = 0.25. Despite, G_2 having the same expression as G_1 , i.e.

$$G_2^{Th}(k_1, M) = |\underline{\Lambda}_{\mathbb{N}}|$$

$$= \left| e^{-2\pi i M} \overline{\Lambda}_{\mathbb{N}} - \frac{i\sqrt{i}}{M\Gamma(2M)} \sqrt{\frac{\pi}{2}} \left(\frac{k_1}{1+M} \right)^{(1/2)+2M} e^{-i\pi M} \overline{\Lambda}_{\mathbb{M}} \right| \quad (3.43)$$

the initial conditions in the momentum perturbation case lead to $\overline{\Lambda}_{\rm N} \sim \overline{\Lambda}_{\rm M} \sim 1$, making the second term in the growth a function of $k_1^{(1/2)+2M}$.

4. WKB analysis for viscous gases

4.1. Weakly viscous regime
$$Re \sim k_1^2$$

For simplicity, we presented the WKB analysis in the previous section for an inviscid gas. Since the growth of the perturbation obtained in the inviscid analysis increases with increasing wavenumber, it is important to assess the role of viscous effects in limiting the growth and establishing a most amplified perturbation. Thus, we will now generalise the analysis for finite Reynolds numbers. In the outer regions, the number density satisfies (3.1) with the coefficients

$$A(t) = -2\frac{k_2k_1}{k_2} - \frac{1+2M}{1+M}ik_2 + \frac{k^2}{(1+M)Re}$$

$$= k_1 \left(i\frac{1+2M}{1+M}t + \frac{1}{k_1}\frac{2t}{1+t^2} + \frac{k_1}{Re}\frac{1+t^2}{1+M} \right)$$

$$= k_1 \left(a_0(t) + \frac{1}{k_1}a_1(t) + \frac{k_1}{Re}a_{Re}(t) \right)$$

$$B(t) = i \left(\frac{1+3M}{1+M}k_1 + \frac{2}{1+M}\frac{k_2^2k_1}{k^2} + \frac{M}{1+M}ik_2^2 - \frac{k^2k_2}{(1+M)Re} \right)$$

$$= ik_1^2 \left(i\frac{M}{1+M}t^2 + \frac{1}{k_1}\left(\frac{2}{1+M}\frac{t^2}{1+t^2} + \frac{1+3M}{1+M} \right) + \frac{k_1}{Re}\frac{t(1+t^2)}{1+M} \right)$$

$$= k_1^2 \left(b_0(t) + \frac{1}{k_1}b_1(t) + \frac{k_1}{Re}b_{Re}(t) \right). \tag{4.2}$$

It is clear that the magnitude of k_1/Re controls the order at which the functions a_{Re} and b_{Re} enter the WKB expansion. When $k_1/Re = O(1/k_1^n)$ with $n \ge 2$, the viscous effects are too small to impact the first two orders S_0 and S_1 . In such cases, the inviscid analysis presented earlier is accurate. On the other hand, a Reynolds number such that $k_1/Re = O(1/k_1)$, is small enough to change the equation for S_1 , but leaves S_0 unchanged. For this case, which we term weakly viscous, the viscous damping influences the amplitude of the outer solution while leaving the frequency unchanged. The weakly viscous case, $Re = O(k_1^2)$ corresponds to a dimensional wavelength in the outer region on the order of the distance, $(\nu/\Gamma)^{1/2}$, that viscous diffusion of

momentum occurs during the turning of the wave by the shear in the outer region. The equations for the WKB expansion are now (3.6) and

$$S''_{0} + 2S'_{0}S'_{1} + a_{0}S'_{1} + \left(a_{1} + \frac{k_{1}^{2}}{Re}a_{Re}\right)S'_{0} + b_{1} + \frac{k_{1}^{2}}{Re}b_{Re} = 0.$$
 (4.3)

Proceeding as in the previous analysis, we derive two modes which now account for the viscous terms:

$$\hat{n}^{M}(t) = \frac{1}{|t|^{2M+1}} \frac{1}{(1+t^{2})^{1-M}} \exp\left(-i\frac{M}{1+M}k_{1}\frac{t^{2}}{2}\right) \exp\left(-\frac{k_{1}^{2}}{Re(1+M)}t\left(1+\frac{t^{2}}{3}\right)\right)$$
(4.4)
$$\hat{n}^{N}(t) = \left(\frac{t^{2}}{1+t^{2}}\right)^{M} \exp\left(-ik_{1}\frac{t^{2}}{2}\right).$$
(4.5)

The number density mode is not influenced by the Reynolds number and remains the same as that in the inviscid analysis. The momentum mode has the same form as that for the inviscid analysis except for the final term giving viscous damping in terms of an exponential function of k_1 , Re, M and t. The damping is more rapid when the wavevector is nearly vertical (large |t|) and becomes asymptotically small as one approaches the turning point $|t| \sim O(1/k_1^{1/2})$, because the wavelength over which viscous diffusion must occur becomes smaller as $|t| \to \infty$ and larger as $|t| \to 0$. The lack of damping of the number density mode indicates that even in a viscous gas, the disturbance does not decay at long times and one is left with a finite long time number density fluctuation. Since it has been found that the most amplified perturbations are those in which an initial momentum perturbation triggers a number density wave in the turning point, the damping of the M mode will play an important role in limiting the maximum growth that can be achieved.

Consistent with our observation that damping of the outer solution becomes negligible as one approaches the inner region $|t| \sim O(1/k_1^{1/2})$ in the weakly viscous limit $Re = O(k_1^2)$, we will see that the inner solution remains unaltered from the inviscid analysis in § 3.3 for this case. Thus, one can still use the matching relations (3.39) to relate the coefficients of the upstream and downstream outer region modes. In figure 12(a,b), we show a comparison of the weakly viscous outer solution with the numerical solution for examples within the weakly viscous regime corresponding to initial velocity and number density perturbations, respectively. The theory yields an accurate prediction of the variation of the amplitude with time.

4.2. Moderately viscous regime,
$$Re \sim k_1^{3/2}$$

At a sufficiently small Reynolds number, viscous effects will begin to influence the solution even during the relatively short time period of the turning point. To examine these viscous effects we repeat the procedure for deriving the turning point approximation by transforming (3.1)–(3.34) using the transformation (3.33), and doing a Taylor series expansion of g, keeping in mind that time scales as $t = O(1/\sqrt{k_1})$ in the inner region. It is found that no viscous terms arise when $Re = O(k_1^2)$. However, if we perform this analysis for a Reynolds number that scales as $Re = O(k_1^{3/2})$, we obtain

$$g(\tau) = \frac{1}{k_1} \left\{ \frac{1}{4(1+M)^2} \left(\tau + \frac{ik_1^{3/2}}{Re} \right)^2 + i\frac{1+4M}{2(1+M)} + O\left(\frac{1}{k_1}\right) \right\}$$
(4.6)

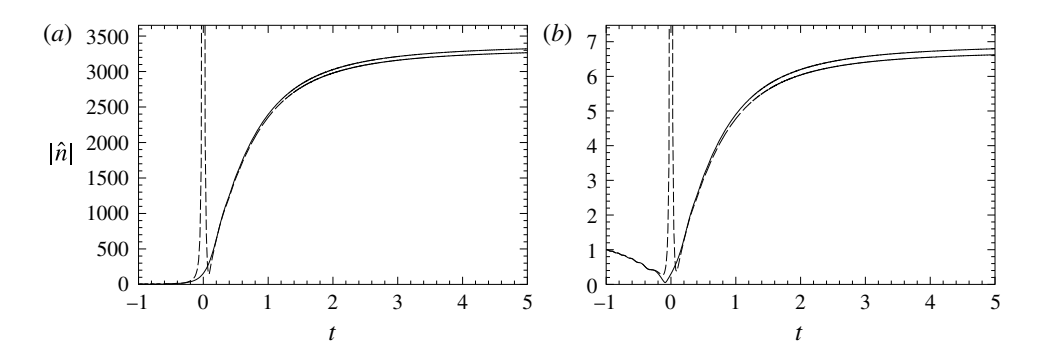


FIGURE 12. Comparison between theory (dashed line) and simulation (solid line) for the parameters $k_1 = 125$, $k_2 = k_1 = 125$, M = 0.5, $Re = k_1^2 = 15625$ and different initial conditions: (a) $\hat{n}(t = t_0) = 0$, $\hat{u}_2(t = t_0) = 1$; (b) $\hat{n}(t = t_0) = 1$, $\hat{u}_2(t = t_0) = 0$. The initial configuration is $k_2(t_0) = k_1$. Only the two outer WKB solutions are represented.

where $\tau = tk_1^{1/2}$. The resulting equation takes the form of a parabolic cylinder equation in terms of a complex shifted time variable:

$$\frac{d^2x}{dT^{*2}} + (T^{*2} + \lambda)x = 0 \tag{4.7}$$

where $T^* = \sqrt{(k_1/(2(1+M)))}t^*$, $t^* = t + \mathrm{i}k_1/Re$ and $\lambda = \mathrm{i}(1+4M)$. Viscous effects would not alter the matching the coefficients of the waves in the upstream and downstream outer regions because, in the matching region corresponding to $|t| \gg 1/\sqrt{k_1}$, the complex shift can be neglected and $t^* \simeq t$. However, viscous effects in the inner region do alter the response to a wave produced by a momentum initial condition within the inner region. We may then expect viscous effects to scale with $Re/k_1^{3/2}$ for an initial fluid velocity disturbance whose wavevector is horizontal. This prediction of the analysis is corroborated by the numerical solution presented in figure 13.

To summarise, viscosity affects the results in three different parameter regimes. For very high Reynolds number Re and moderate wavenumbers such that $k_1 \ll Re^{1/2}$, viscosity plays no role and the dynamics can be described by the inviscid equations. The growth of the disturbance for this range of wavenumbers is a power law of k_1 . The weakly viscous case occurs for higher wavenumbers such that $k_1 \sim Re^{1/2}$ and $k_1 \ll Re^{2/3}$. Damping of the M mode, for these waves, happens in the outer regions only, but the N mode is unaffected by viscosity. Since the inner region creates the N mode responsible for the long-term saturation from an incoming M mode, waves that start far enough upstream for some amplification of the incoming M mode but without too much viscous damping lead to the largest growth. Next, viscous effects cause strong damping of the M mode in the outer region and begin to have an effect even in the inner region for wavenumbers of order $Re^{2/3}$. In this case, the largest growth is seen for initial conditions with nearly horizontal wavenumbers, although this growth is much smaller than for the weakly viscous case. Finally, if $k_1 \gg Re^{2/3}$ viscosity dominates in both the inner and outer regions and only the N mode survives providing a disturbance that neither grows nor decays with time.

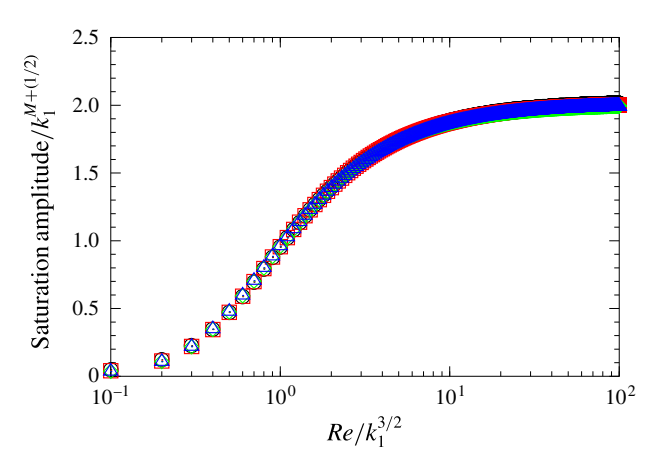


FIGURE 13. (Colour online) Saturation amplitude of number density for initially horizontal waves with initial conditions $\hat{n} = 0$, $\hat{u}_2 = 1$. The mass loading is M = 0.5. The amplitudes are obtained numerically with the symbols referring to $k_1 = 50$ (\odot), 75 (\square), 100 (\diamondsuit), 125 (\triangle).

4.3. Growth of the perturbations at finite Re

To assess quantitatively the growth at finite Reynolds numbers, we consider again the growth functions G_1 , due to a number density perturbation initial condition, and G_2 , due to a momentum perturbation initial condition, defined in (3.40). The theoretical growth based on the solutions we found is given in (3.42) and (3.43). For the sake of clarity, we reproduce the equality below

$$G_{i}^{Th}(k_{1}, M, Re, t_{0}) = \left| \underline{\Lambda}_{\mathbb{N}} \right|$$

$$= \left| e^{-2\pi i M} \overline{\Lambda}_{\mathbb{N}} - \frac{i\sqrt{i}}{M\Gamma(2M)} \sqrt{\frac{\pi}{2}} \left(\frac{k_{1}}{1+M} \right)^{(1/2)+2M} e^{-i\pi M} \overline{\Lambda}_{\mathbb{M}} \right|. \quad (4.8)$$

The coefficients $\overline{\Lambda}_{\mathbb{N}}$ and $\overline{\Lambda}_{\mathbb{N}}$ for the initial conditions $(\hat{n}|_{t_0} = 1 \text{ and } \hat{u}_2|_{t_0} = 0)$ are found to be

$$\overline{\Lambda}_{N} \simeq \frac{1}{\hat{n}_{N}(t_{0})}
\overline{\Lambda}_{M} \simeq \frac{i2M(1+M)}{k_{1}t_{0}^{2}(1+t_{0}^{2})} \frac{1}{\hat{n}_{M}(t_{0})}.$$
(4.9)

Note that $|\hat{n}_{\rm M}(t_0)| \sim \exp(k_1^2/Re(1+M))$ for $t_0 < 0$ and $|t_0| = O(1)$ which can be very large if Re/k_1^2 is small. The expressions above show that the growth has a contribution $|\overline{\Lambda}_{\rm N}|$ that comes from the N mode prior to the turning point and that depends on Re/k_1^2 only. An additional contribution comes from the M mode prior to the turning point, $|k_1^{(1/2)+2M}\overline{\Lambda}_{\rm M}|$ that varies like $k_1^{-(1/2)+2M}$ times a function of Re/k_1^2 . In figure 14(a), we compare the simulated and predicted growth normalised by $k_1^{-(1/2)+2M}$ as a function of Re/k_1^2 . This scaling collapses the results partially but not completely because the N mode contribution plays comparable role to the M mode contribution for the wavenumbers considered and does not scale as $k_1^{-(1/2)+2M}$.

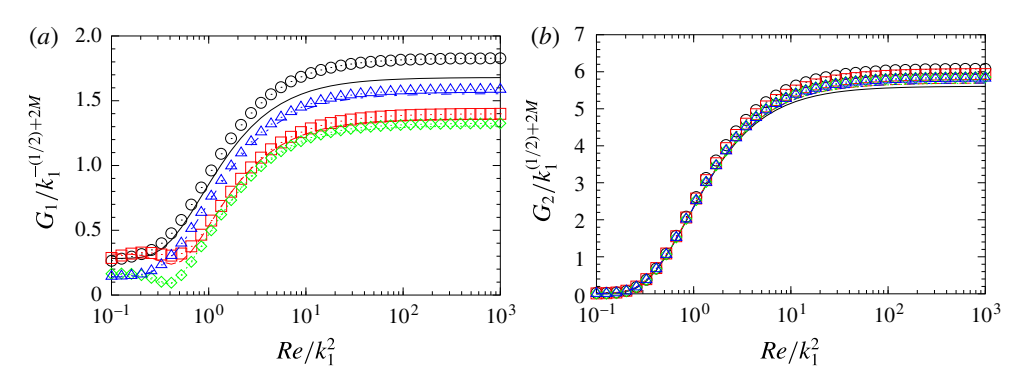


FIGURE 14. (Colour online) Growth functions G_1 and G_2 normalised based on the theoretical predictions for the given initial conditions versus Re/k_1^2 , for a mass loading M=0.5. Symbols correspond to simulations and lines to theoretical values. The wavevector is initially at an angle 45° upstream $(t_0=-1)$, with $k_1=25$ (——/ \odot), 50 (——/ \odot), 75 (···/ \diamondsuit), 100 (— ·—/ \bigtriangleup).

The second set of initial conditions $(\hat{n}|_{t_0} = 0 \text{ and } \hat{u}_2|_{t_0} = 1)$ yields

$$\overline{\Lambda}_{N} \simeq -\frac{2(1+M)}{t_{0}} \frac{1}{\hat{n}_{N}(t_{0})}
\overline{\Lambda}_{M} \simeq \frac{2(1+M)}{t_{0}} \frac{1}{\hat{n}_{M}(t_{0})}.$$
(4.10)

In this case the N mode contribution is negligible and the results are dominated by M mode contribution that scales as $k_1^{(1/2)+2M} \exp(k_1^2/Re(1+M))$ for a $t_0 < 0$ and $|t_0| = O(1)$. We test this scaling in figure 14(b) where we reported $G_2(k_1, M, Re, t_0)/k_1^{(1/2)+2M}$ for different values of k_1 as a function of Re/k_1^2 and for $t_0 = -1$. We observe that for all values of k_1 , the curves collapse proving, that the growth normalised by $k_1^{(1/2)+2M}$ varies solely with the ratio Re/k_1^2 for high k_1 and fixed mass loading M and initial time t_0 .

In general, the initial wavevector of the perturbations can have any direction. In the inviscid case $Re = \infty$, the growth can take arbitrary large values as $|t_0| = |k_2/k_1|$ increases for $t_0 < 0$. A finite Reynolds number will, however, set a limit to the growth and will damp M modes with sufficiently large values of $|t_0|$ before they reach the turning point where they can induce an N mode. The optimal starting configuration leading to the most growth will then depend on the mass loading, Reynolds number, and the horizontal component of the wavenumber. The corresponding optimal growth for a set of parameters is given by

$$\sup_{t_0} G_i(k_1, M, Re) \tag{4.11}$$

and is met for an ideal initial configuration $-t_0^{opt} = (k_2/k_1)^{opt}$.

The isocontours of sup G_1 and sup G_2 in (k_1, Re) space obtained from numerical solution of the differential equations are presented in figure 15 for a mass loading M = 0.5 along with the corresponding plot of the optimal $|t_0|$. As suggested by the previous discussion, the plots show that k_2/k_1 tends to zero, i.e. towards the inner

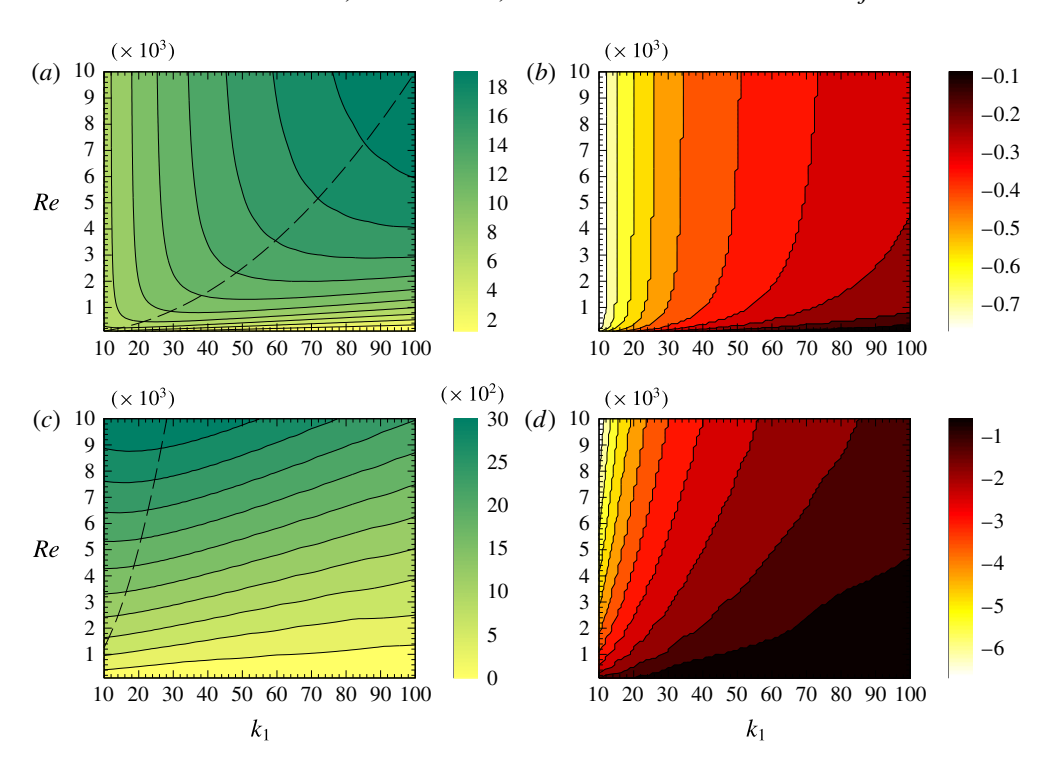


FIGURE 15. (Colour online) Isocontours of the growth functions in (k_1, Re) space: (a) $\sup_{t_0} G_1$ for M = 0.5; (b) t^{opt} for M = 0.5; (c) $\sup_{t_0} G_2$ for M = 0.5; (d) t^{opt} for M = 0.5. The dashed line is $Re = k_1^2$ in (a) and $Re = 12.6k_1^2$ in (c).

region, as the Reynolds number goes to zero. The locations of the most amplified wavenumbers follow roughly the $Re \sim k_1^2$ scaling for $\sup G_1$ and $Re \sim 12.6k_1^2$ for $\sup G_2$ that one would expect based on the weakly viscous analysis.

To obtain theoretical predictions for the most amplified mode for a given Re and M, one can solve $\partial G_i/\partial k_1 = \partial G_i/\partial t_0 = 0$. We focus on the case of an initial momentum disturbance, since it leads to the highest growth. For $k_1 \gg 1$, one can use the approximate expression G_2^{Th} given in (3.43) (we neglect the N mode contribution as justified previously) combined with the expressions for the coefficient Λ_N in (4.10). Maximising the growth leads to an optimal initial time satisfying

$$\left(2M - \frac{5}{6}\right)t_0^4 + \left(\frac{8}{3}M - 3\right)t_0^2 + \frac{1}{2} - 2M = 0\tag{4.12}$$

and a corresponding optimal k_1^{opt} given by the relation

$$Re = -\frac{4t_0(1 + t_0^2/3)}{(1 + 4M)(1 + M)}k_1^2. \tag{4.13}$$

For mass loadings larger than 5/12, the optimum time given by (4.12) can be written as

$$t_0^{opt} = -\sqrt{\frac{8/3M - 3 - 4/3\sqrt{13M^2 - 15M + 6}}{5/3 - 4M}}. (4.14)$$

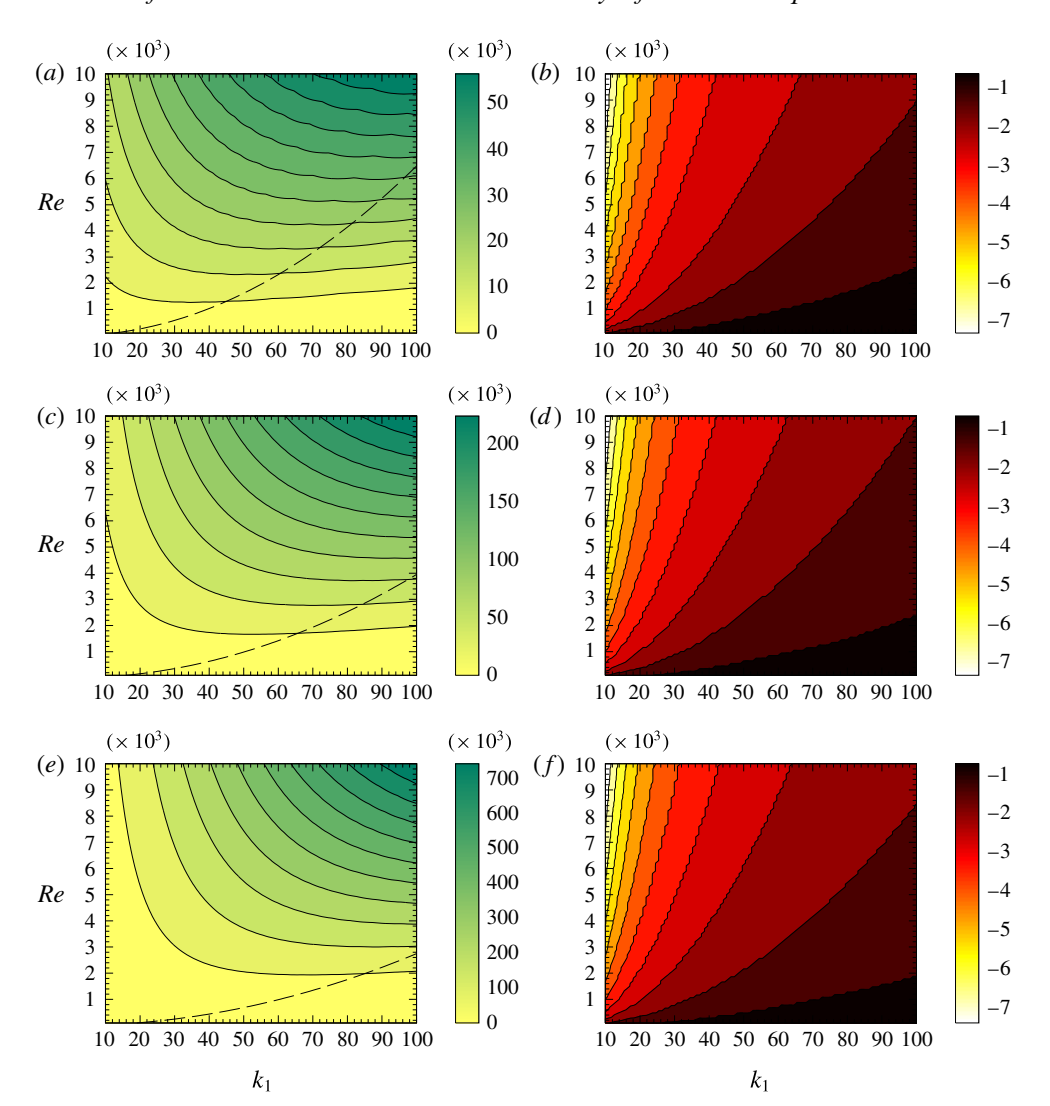


FIGURE 16. (Colour online) Isocontours of $\sup_{t_0} G_2$ in (k_1, Re) space with the corresponding t_0^{opt} obtained from simulations: (a) $\sup_{t_0} G_2$ for M = 1; (b) t^{opt} for M = 1; (c) $\sup_{t_0} G_2$ for M = 1.25; (d) t^{opt} for M = 1.25; (e) $\sup_{t_0} G_2$ for M = 1.5; (f) t^{opt} for M = 1.5. The dashed line represent the most amplified wavenumbers obtained using (4.14) and (4.13).

In the case of mass loading M = 0.5, this time is $t^{opt} = -3.2$. Using the relation (4.13) we obtain $Re = 12.63k_1^2$ in agreement with the numerical solutions.

For mass loadings smaller than 5/12, the most amplified mode is obtained when $t_0 \to -\infty$ and $k_1 \to 0$. For such small wavenumbers, the expression (3.43) is no longer valid and one can only conclude that small wavenumbers, not captured by the WKB method, can lead to higher growth than the larger wavenumbers. Figure 16 demonstrates that the relations (4.13) and (4.14) are able to predict the optimal wavenumber and initial orientation for mass loadings M = 1, 1.25 and 1.5. Note that the growth is very large for these cases which might have implications on the

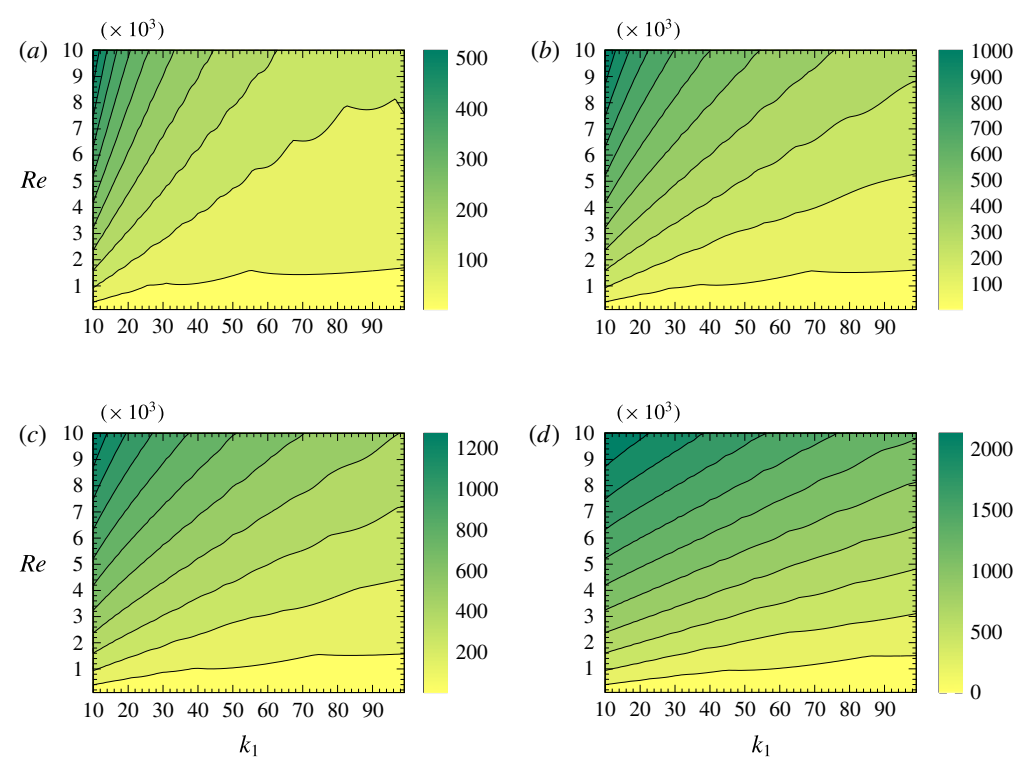


FIGURE 17. (Colour online) Isocontours of $\sup_{t_0} G_2$ for four different mass loadings smaller than $5/12 \sim 0.466$: (a) M = 0.125; (b) M = 0.25; (c) M = 0.3; (d) M = 0.46. The isocontours are obtained from simulations.

development of nonlinearities. Figure 17 shows that for the mass loadings smaller than $5/12 \sim 0.46$ (here M = 0.125, 0.25, 0.3 and 0.46) the most amplified wavenumber at a given Reynolds number is below $k_1 = 10$, corroborating our theoretical argument that small wavenumbers are most amplified for such small mass loadings.

5. Conclusion

The stability of a gas-solid suspension with small but non-zero Stokes numbers subject to a homogeneous shear has been investigated with a linear stability analysis. The complete description of rotating wave-like perturbations, analogous to the Kelvin modes for single phase flow, has been detailed. A WKB asymptotic analysis yielded analytical results for cases where the initial wavelength of the perturbation is smaller than the characteristic particle settling distance in a shear time scale: $L = U_g/\Gamma$, the case that was shown to yield the largest growth for mass loadings M > 5/12. The theory is applicable for order-one mass loadings for which analytical solutions were shown to replicate numerical simulations with excellent agreement. The instability presented in this paper can be considered as one of the few building-block instabilities available to enhance our qualitative understanding of the mechanics of dispersed multiphase flows.

To model the gas-solid suspension, a small Stokes approximation of the particle velocity field (2.5) was used in addition to a momentum coupling between the two

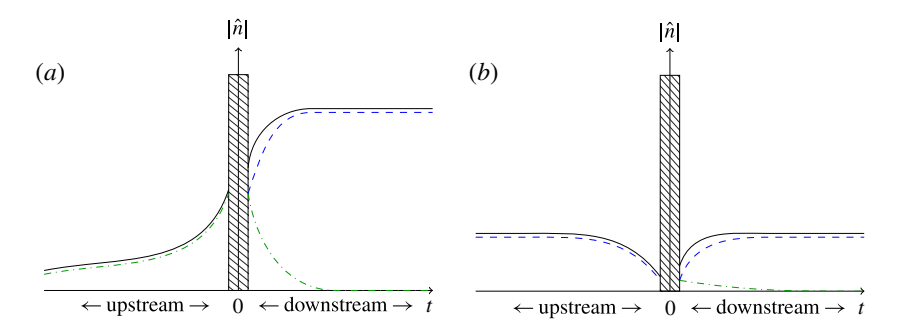


FIGURE 18. (Colour online) Two schematics depicting the evolution of the N (dashed/blue online) and M (dash-dotted/green online) modes from upstream to downstream. The solid black curve represents the total perturbation, which is a linear combination of the two modes. (a) Evolution of the disturbance due to an upstream M mode: the mode grows until it reaches the inner region, which results in the generation of a N mode in the downstream region. The latter grows to a saturation amplitude $k_1^{(1/2)+2M}$ times higher than the upstream mode that created it. The downstream M mode vanishes with time. (b) Evolution of the disturbance due to an upstream N mode: the mode decays until it reaches the inner region, which results in the generation of a small M mode in the downstream region. The latter decays and the downstream N reaches a saturation amplitude similar to the starting one. There is no overall amplification due to an upstream N mode.

phases as described for dilute suspensions in Druzhinin (1995) (2.2). The resulting number density equation features preferential concentration, a term that acts as a sink in high-vorticity regions of the flow and as a source in high-stretching regions (2.9). The feedback of the particles on the fluid momentum is via a gravitational forcing term in (2.8) that depends on the effective local suspension density $\rho_{eff} = \rho_f + m_p n$. This coupled action is critical to the maintenance and growth of a perturbation. The latter is chosen as a rotating wave, a class of perturbations relevant to the study of unbounded homogeneous shear, and first introduced in Kelvin (1887). Such a perturbation is characterised by its initial wavevector which for two-dimensional perturbations is $(k_1, k_2(t))$. This wavevector evolves with time and eventually aligns along the mean velocity gradient (2.20).

For the case when gravity is parallel to the velocity gradient, we have used the WKB analysis valid for $k_1\gg U_g/\Gamma$ two identify two solutions, which are termed the number density (N) mode and the momentum (M) mode. Analytical expressions for the modes are given by (3.15)–(3.18), (4.5) and (4.4). Any small perturbation can be expressed as a linear combination of the two modes, when the wavevector has an orientation far from the horizontal with $|k_2|\gg\sqrt{k_1\Gamma/U_g}$. As the wave rotates under the base shear, and goes from an upstream configuration $k_2(t)/k_1>0$ to a downstream configuration $k_2(t)/k_1<0$, there is a very narrow range of configurations $|k_2|=O(\sqrt{k_1\Gamma/U_g})$, referred to as the inner region, where the solution is given in terms of parabolic cylinder functions. As the wave passes across this inner region the upstream N and M mode can each produce both a downstream N and M mode. This particular point is critical to the growth of perturbations.

The sketch in figure 18 shows the evolution of disturbances produced by an initial momentum mode (figure 18a) and an initial number density mode (figure 18b). In § 3.2, we discussed the manner in which preferential concentration, gravitational forcing and the relative propagation of momentum and number density disturbances

due to settling lead an N mode to decay upstream and grow downstream of the turning point, while an M mode grows upstream and decays downstream of the turning point (see figures 8 and 9). As shown in figure 18(b), an initial N mode decays until reaching the turning point and produces at the turning point an N that manages to return to the initial amplitude and a small M that decays. In contrast the initial M mode illustrated in figure 18(a) grows in the upstream region and produces at the turning point a downstream N mode that grows further and saturates at a large finite amplitude as $t \to \infty$. As a result the largest growth occurs due to initial fluid velocity disturbances which produce large number density disturbances as the wave turns.

The inviscid analysis in § 3 shows that an initial velocity disturbance leads to a downstream N mode with an amplification factor of $(U_{\nu}k_1/\Gamma)^{(1/2)+2M}$ that grows algebraically with decreasing wavelength when the wavelength is much smaller than the distance U_{ϱ}/Γ that particles settle during the shearing time scale, i.e. $k_1 \gg \Gamma/U_{\varrho}$. However, when viscous diffusion can transfer momentum across the wavelength during the shearing time, i.e. $vk_1^2/\Gamma = O(1)$, viscous effects begin to damp the M mode as shown in § 4. As a result the maximum amplification occurs at a wavenumber $k_1 = O((\Gamma/\nu)^{1/2})$ and a wave orientation $k_2/k_1 = O(1)$ which is determined as a function of the mass loading in (4.14). The optimal wavelength is small compared with the settling distance U_g/Γ and the WKB analysis predicts the maximum growth wavevector analytically provided that M > 5/12. For smaller mass loading, the optimal wavelength is $O(U_g/\Gamma)$ and a numerical solution of the linearised equations is required to determine its value. Large-wavenumber momentum disturbances with $k_1 \gg (\Gamma/\nu)^{1/2}$ are greatly damped before reaching the turning point. At these wavenumbers, the most amplified wavevector orientation is near the horizontal in the turning point region. Initial disturbances with horizontal wavenumbers are finally damped at a still higher wavenumber $k_1 = O((\Gamma U_g)^{1/3} v^{2/3})$ for which viscous effects become important in the turning point region, cf. figure 13. Nonetheless, the largest growth occurs for disturbances with $k_1 = O((\Gamma/\nu)^{1/2})$ and $k_2/k_1 = O(1)$ as given by (4.14) and (4.13).

It would be natural to expect that an instability involving preferential concentration of particles and their gravitational forcing of the gas flow might lead to an enhancement of the particle settling rate. While the extent to which this ultimately occurs depends on the nonlinear evolution of the number density and velocity perturbations, some indication of the initial change in settling velocity for small perturbations can be gleaned from the linear stability analysis. The phase-averaged vertical particle velocity is

$$\langle v_2 \rangle = \boldsymbol{e}_2 \cdot \frac{\int_0^{2\pi} \operatorname{Re}\{n(\boldsymbol{x}, t)\} \operatorname{Re}\{\boldsymbol{v}(\boldsymbol{x}, t)\} d\xi}{\int_0^{2\pi} n_0 d\xi}$$
 (5.1)

where $\xi = \mathbf{k} \cdot \mathbf{x}$ is a spatial coordinate parallel to the wavevector and Re{} is the real part of a complex number. In presence of the perturbations the average particle velocity differs from $-U_g$ by

$$\Delta \langle v_2 \rangle = \langle v_2 \rangle - (-U_g) = \frac{St}{2\pi} \text{Re}\{\hat{u}_2 \hat{n}^*\}.$$
 (5.2)

The star here denotes the complex conjugate. The scaled change in the particle velocity is plotted as a function of time in figure 19. The change of the particle velocity

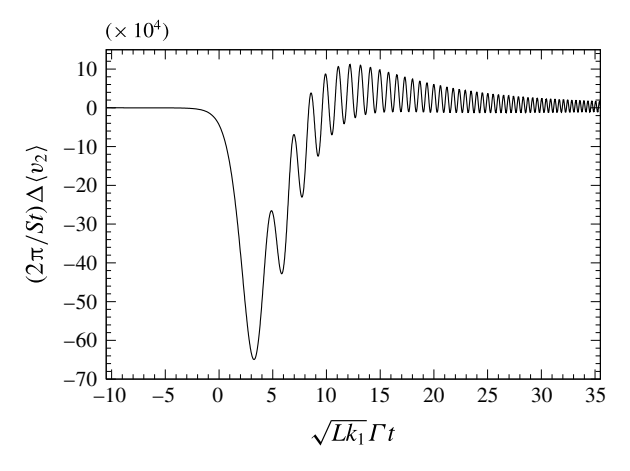


FIGURE 19. Change in the particle velocity due to perturbations with the scaled initial conditions $\hat{u}_2 = 1$, $\hat{n} = 0$ for the parameters $U_g k_1 / \Gamma = 100$, M = 1, and $Re = \infty$. The change is scaled with the small amplitude of the initial perturbation.

averaged over a period of oscillation is zero in the outer region $(|\sqrt{Lk_1}\Gamma t|\gg 1)$. However, in the inner region $(|\sqrt{Lk_1}\Gamma t|\leqslant 10)$, i.e. when the number density streaks are vertical and the coupling between the velocity perturbation and particle phase is strongest, there is a net enhancement of the settling rate. In the absence of a secondary instability, the increase of the settling velocity is transient and one can characterise its effects in terms of the net extra displacement a particle experiences as the wavevector passes through the turning point. This extra displacement for the parameters considered in figure 19 is

$$\Delta \langle r_2 \rangle_{t_0} = \int_{-1}^{\infty} \Delta \langle v_2 \rangle \frac{1}{\Gamma} d(\Gamma t) \sim -2.7 \times 10^4 u' \tau_p \tag{5.3}$$

in which u' is the magnitude of the initial velocity perturbation, which should be small compared with U_g in the context of linear theory. Thus, the instability leads to a downward displacement that is by many orders of magnitude larger than the displacement an inertial particle might experience due to the initial perturbation.

Despite its algebraic nature, the instability presented in this paper can amplify disturbances by a significant amount. To illustrate this, consider the example of a suspension of 80 μ m diameter silica particles in sheared air at standard pressure and temperature with $\Gamma=1.5~{\rm s}^{-1}$. The particle Stokes number is St=0.07. With a volume fraction $\phi=4.6\times 10^{-4}$, the suspension mass loading is M=1. The Reynolds number is $Re=U_g^2/(\Gamma\nu)=11\,690$. Under these conditions, an initial perturbation to the velocity field with a wavelength $\lambda=1.1$ cm oriented 56° upstream leads to an amplification of four orders of magnitude (7.4×10^4) despite some viscous effects $(Re/(Lk_1)^2\sim 1)$.

It has long been hypothesised that transient linear growth can explain the transition to turbulence in flows that are otherwise unconditionally stable from the stand point of traditional linear analysis, such as flows in circular pipe. Several research groups wave worked on means of identifying optimal transient perturbations (Trefethen *et al.* 1993; Trefethen 1997; Schmid 2007), and it has been shown by Baggett & Trefethen (1997) that an optimal transient mode that achieves a growth of 1.5–2 orders of magnitude

120

can trigger nonlinearities leading to significantly higher magnifications. This effect is known as bootstrapping. The instability presented in this paper, although of finite amplitude, is able to achieve a growth of four orders of magnitude and more, which makes us believe that it might achieve even higher growth by bootstrapping.

In the present mechanism the large finite-amplitude disturbance that is created is not transient but persists at long times allowing even more opportunity for the onset of secondary instabilities than in cases such as single-phase pipe flow. Once a wave is amplified and turned by the shear, the final state is a periodic number density stratified vertically. Such a configuration is subject to a Rayleigh–Taylor instability as described in Batchelor & Nitsche (1991). While the shear mechanism converts, for the most part, a momentum perturbation into a number density perturbation, a secondary Rayleigh–Taylor instability converts a number density perturbation back to a momentum one while resetting the wave orientation to a direction that is not parallel to gravity. A second cycle of shear and Rayleigh–Taylor instability may then be expected to take place to further reinforce the perturbation. Whether, these two instabilities take place simultaneously or sequentially will depend on the size of the initial disturbance and their respective growth rates.

While we have considered the idealised case of the instability of a homogeneously sheared gas–solid suspension, this analysis will be applicable to disturbances that are small in comparison with the distance over which the shear rate varies in a more complex flow. As an example, consider a mixing layer in which two fluid streams with velocity difference ΔU have interacted long enough to develop a shear layer of thickness δ . The shear rate in this layer will be $\Gamma = O(\Delta U/\delta)$ and the Reynolds number of the shear layer is $Re_{SL} = \Delta U\delta/\nu = \Gamma\delta^2/\nu$. The current analysis predicts that, in the presence of particles settling across this mixing layer, a fluid velocity disturbance will lead to a large growth of particle concentration fluctuations with an optimal wavelength $\lambda = 2\pi/k_1 = O((\nu/\Gamma)^{1/2})$. This optimal wavelength is much smaller than the shear layer thickness $\delta = (\nu/\Gamma)^{1/2}Re_{SL}^{1/2}$ for any high-Reynolds-number shear layer. Thus, the dominance of small-wavelength disturbances that justifies the use of the WKB analysis makes the analysis applicable to the consideration of local disturbances in many complex flows.

Acknowledgement

This work was supported by NSF grant CBET-1233793.

Appendix A. Inviscid solution in the inner region

Gradshteyn *et al.* (2000) provide asymptotic relationships for the behaviour of the parabolic cylinder functions as $T \to \pm \infty$ and this facilitates the derivation of analytical relationships between the amplitudes of the upstream and downstream modes. To match the upstream outer region $(t \lesssim -1)$ to the turning point, consider the asymptotic expansion of the parabolic cylinder functions for times such that $t \leqslant 0$ and $|T| \gg 1$:

$$\begin{split} D_{2M}[(1+\mathrm{i})T] &\simeq 2^M \mathrm{e}^{-\mathrm{i}((3\pi)/2)M} \mathrm{e}^{-\mathrm{i}(T^2/2)} |T|^{2M} \\ &+ \frac{\sqrt{2\pi}}{\Gamma(-2M)} \mathrm{e}^{-\mathrm{i}\pi(M/2)} \mathrm{e}^{-\mathrm{i}(\pi/4)} \frac{1}{2^{(1/2)+M}} + \frac{\mathrm{e}^{\mathrm{i}T^2/2}}{|T|^{1+2M}} \end{split} \tag{A 1}$$

$$D_{2M}[-(1+i)T] \simeq 2^M e^{i(\pi/2)M} e^{-i(T^2/2)} |T|^{2M}.$$
 (A 2)

Preferential concentration driven instability of sheared suspensions

121

Using these expansions, the inner solution for $t \le 0$ and $|t| \gg 1/\sqrt{k_1}$ approaches

$$\hat{n}(t) \simeq \left(\frac{k_1}{1+M}\right)^M \left(\Lambda_+ e^{-i((3\pi)/2)M} + \Lambda_- e^{i(\pi/2)M}\right) |t|^{2M} e^{-ik_1(t^2/2)}$$

$$+ \Lambda_+ \frac{\sqrt{2\pi}}{\Gamma(-2M)} e^{-i(\pi/2)M} e^{-i(\pi/4)} \left(\frac{1+M}{k_1}\right)^{(1/2)+M} \frac{e^{-i(M/(1+M))k_1(t^2/2)}}{|t|^{2M+1}}. \quad (A3)$$

Note that the asymptotic expressions for the upstream N and M modes when $|t| \ll 1$ are

$$\hat{n}^{N} \sim |t|^{2M} e^{-ik_1(t^2/2)}$$
 (A 4)

$$\hat{n}^{\text{M}} \sim \frac{1}{|t|^{2M+1}} e^{-i(M/(1+M))k_1(t^2/2)}.$$
 (A 5)

It is seen that the functional form of the parabolic cylinder functions is consistent with that of the N and M modes within the matching region t < 0 and $1/\sqrt{k_1} \ll |t| \ll 1$ provided that we relate the coefficients as

$$\overline{\Lambda}_{N} = \left(\frac{k_{1}}{1+M}\right)^{M} \left(\Lambda_{+} e^{-i((3\pi)/2)M} + \Lambda_{-} e^{i(\pi/2)M}\right)
\overline{\Lambda}_{M} = \Lambda_{+} \frac{\sqrt{2\pi}}{\Gamma(-2M)} e^{-i(\pi/2)M} e^{-i(\pi/4)} \left(\frac{1+M}{k_{1}}\right)^{(1/2)+M}.$$
(A 6)

A similar matching of the inner solution with the downstream outer solution in the matching region $1 \gg t \gg 1/\sqrt{k_1}$ yields

$$\underline{\Lambda}_{N} = \left(\frac{k_{1}}{1+M}\right)^{M} \left(\Lambda_{-} e^{-i((3\pi)/2)M} + \Lambda_{+} e^{i(\pi/2)M}\right)$$

$$\underline{\Lambda}_{M} = \Lambda_{-} \frac{\sqrt{2\pi}}{\Gamma(-2M)} e^{-i(\pi/2)M} e^{-i(\pi/4)} \left(\frac{1+M}{k_{1}}\right)^{(1/2)+M}.$$
(A 7)

The coefficients of the downstream modes can therefore be expressed in terms of the amplitudes of the upstream modes as

$$\underline{\Lambda}_{\rm N} = -\frac{\mathrm{i}\sqrt{\mathrm{i}}}{M\Gamma(2M)}\sqrt{\frac{\pi}{2}}\left(\frac{k_1}{1+M}\right)^{(1/2)+2M}\mathrm{e}^{-\mathrm{i}\pi M}\overline{\Lambda}_{\rm M} + \mathrm{e}^{-2\pi\mathrm{i}M}\overline{\Lambda}_{\rm N}$$

$$\underline{\Lambda}_{\rm M} = -\mathrm{e}^{-2\pi\mathrm{i}M}\overline{\Lambda}_{\rm M} - \mathrm{i}\sqrt{\mathrm{i}}\sqrt{\frac{2}{\pi}}2M\sin(2M\pi)\Gamma(2M)\mathrm{e}^{-\mathrm{i}\pi M}\left(\frac{1+M}{k_1}\right)^{(1/2)+2M}\overline{\Lambda}_{\rm N}.$$
(A 8)

REFERENCES

ALFARO, S. C. & GOMEZ, L. 2001 Modeling mineral aerosol production by wind erosion: emission intensities and aerosol size distributions in source areas. J. Geophys. Res. 106 (D16), 18075–18084.

ALISEDA, A., CARTELLIER, A., HAINAUX, F. & LASHERAS, J. C. 2002 Effect of preferential concentration on the settling velocity of heavy particles in homogeneous isotropic turbulence. *J. Fluid Mech.* **468**, 77–105; WOS:000178731400003.

- BAGGETT, J. S. & TREFETHEN, L. N. 1997 Low-dimensional models of subcritical transition to turbulence. *Phys. Fluids* **9** (4), 1043–1053.
- BATCHELOR, G. K. 1988 A new theory of the instability of a uniform fluidized bed. *J. Fluid Mech.* **193**, 75–110.
- BATCHELOR, G. K. & NITSCHE, J. M. 1991 Instability of stationary unbounded stratified fluid. *J. Fluid Mech.* 227, 357–391.
- BELLMAN, R. 1997 *Introduction to Matrix Analysis*, 2nd edn. Society for Industrial and Applied Mathematics.
- BENDER, C. M. & ORSZAG, S. A. 1999 Advanced Mathematical Methods for Scientists and Engineers: Asymptotic Methods and Perturbation Theory. Springer.
- CRAIK, A. D. D. & CRIMINALE, W. O. 1986 Evolution of wavelike disturbances in shear flows: a class of exact solutions of the Navier–Stokes equations. *Proc. R. Soc. Lond.* A 406 (1830), 13–26.
- DASGUPTA, S., JACKSON, R. & SUNDARESAN, S. 1994 Turbulent gas-particle flow in vertical risers. AIChE J. 40 (2), 215-228.
- DRUZHININ, O. A. 1995 On the two-way interaction in two-dimensional particle-laden flows: the accumulation of particles and flow modification. *J. Fluid Mech.* **297**, 49–76.
- DYSON, F. J. 1949 The radiation theories of Tomonaga, Schwinger, and Feynman. *Phys. Rev.* **75** (3), 486–502.
- ELGHOBASHI, S. & TRUESDELL, G. C. 1993 On the two-way interaction between homogeneous turbulence and dispersed solid particles. I: turbulence modification. *Phys. Fluids* A **5** (7), 1790–1801.
- FERRY, J. & BALACHANDAR, S. 2001 A fast Eulerian method for disperse two-phase flow. *Intl J. Multiphase Flow* 27 (7), 1199–1226.
- FERRY, J. & BALACHANDAR, S. 2002 Equilibrium expansion for the Eulerian velocity of small particles. *Powder Technol.* **125** (23), 131–139.
- GRADSHTEYN, I. S., RYZHIK, I. M., JEFFREY, A. & ZWILLINGER, D. 2000 Table of Integrals, Series, and Products, 6th edn. Academic.
- HINCH, E. J. 1991 Perturbation Methods. Cambridge University Press.
- KELVIN, L. 1887 Stability of fluid motion: rectilinear motion of viscous fluid between two parallel plates. *Phil. Mag.* **24** (5), 188–196.
- LUN, C. K. K., SAVAGE, S. B., JEFFREY, D. J. & CHEPURNIY, N. 1984 Kinetic theories for granular flow: inelastic particles in Couette flow and slightly inelastic particles in a general flowfield. J. Fluid Mech. 140, 223–256.
- MAGNUS, W. 1954 On the exponential solution of differential equations for a linear operator. *Commun. Pure Appl. Maths* **7** (4), 649–673.
- MAXEY, M. R. & RILEY, J. J. 1983 Equation of motion for a small rigid sphere in a nonuniform flow. *Phys. Fluids* **26** (4), 883–889.
- NISHIMURA, K. & HUNT, J. C. R. 2000 Saltation and incipient suspension above a flat particle bed below a turbulent boundary layer. *J. Fluid Mech.* **417**, 77–102.
- PARTHASARATHY, R. N. & FAETH, G. M. 1990 Turbulence modulation in homogeneous dilute particle-laden flows. *J. Fluid Mech.* **220**, 485–514.
- RANI, S. L. & BALACHANDAR, S. 2003 Evaluation of the equilibrium Eulerian approach for the evolution of particle concentration in isotropic turbulence. *Intl J. Multiphase Flow* **29** (12), 1793–1816.
- SAFFMAN, P. G. 1962 On the stability of laminar flow of a dusty gas. J. Fluid Mech. 13 (01), 120–128.
- SCHMID, P. J. 2007 Nonmodal stability theory. Annu. Rev. Fluid Mech. 39 (1), 129-162.
- SCHMID, P. J. & KYTOMAA, H. K. 1994 Transient and asymptotic stability of granular shear flow. J. Fluid Mech. 264, 255–275.
- SQUIRES, K. D. & EATON, J. K. 1991 Preferential concentration of particles by turbulence. *Phys. Fluids* A **3** (5), 1169–1178.

- TREFETHEN, L. 1997 Pseudospectra of linear operators. SIAM Rev. 39 (3), 383-406.
- TREFETHEN, L. N., TREFETHEN, A. E., REDDY, S. C. & DRISCOLL, T. A. 1993 Hydrodynamic stability without eigenvalues. *Science* **261**, 578–584.
- WANG, C.-H., JACKSON, R. & SUNDARESAN, S. 1996 Stability of bounded rapid shear flows of a granular material. *J. Fluid Mech.* **308**, 31–62.
- WANG, L.-P. & MAXEY, M. R. 1993 Settling velocity and concentration distribution of heavy particles in homogeneous isotropic turbulence. *J. Fluid Mech.* **256**, 27–68.